RESEARCH ARTICLE

ISEV

Systematic compositional analysis of exosomal extracellular vesicles produced by cells undergoing apoptosis, necroptosis and ferroptosis

Benjamin Cappe[1,2] | **Mike Vadi[1,2]** | **Eliza Sack[3]** | **Ludivine Wacheul[3]** |
Bruno Verstraeten[1,2] | **Sara Dufour[4,5,6]** | **Julien Franck[7]** | **Wei Xie[1,2]** |
Francis Impens[4,5,6] | **An Hendrix[8]** | **Denis L. J. Lafontaine[3]** | **Peter Vandenabeele[1,2]** |
Franck B. Riquet[1,2,9]

[1]Cell Death and Inflammation Unit, VIB Center for Inflammation Research, Ghent, Belgium

[2]Department of Biomedical Molecular Biology, Ghent University, Ghent, Belgium

[3]RNA Molecular Biology, Fonds de la Recherche Scientifique (F.R.S./FNRS), Université libre de Bruxelles (ULB), Biopark campus, Gosselies, Belgium

[4]VIB-UGent Center for Medical Biotechnology, VIB, Ghent, Belgium

[5]Department of Biomolecular Medicine, Ghent University, Ghent, Belgium

[6]VIB Proteomics Core, VIB, Ghent, Belgium

[7]University of Lille, Inserm U1192-Laboratoire Protéomique Réponse Inflammatoire Spectrométrie de Masse-PRISM, Lille, France

[8]Laboratory of Experimental Cancer Research, Department of Human Structure and Repair, Ghent University, Ghent, Belgium

[9]University of Lille, CNRS, UMR 8523-PhLAM-Physique des Lasers Atomes et Molécules, Lille, France

Correspondence
Peter Vandenabeele, Cell Death and Inflammation Unit, VIB Center for Inflammation Research, Ghent, Belgium. Email:
peter.vandenabeele@irc.vib-ugent.be

KEY FINDINGS
Comparative analysis in the same cell line of steady-state produced exosomal extracellular vesicles (ssEVs) and cell death-associated exosomal EVs (cdEVs) following TNF-induced necroptosis, anti-Fas-induced apoptosis and ML162-induced ferroptosis revealed that ssEVs and cdEVs contain largely overlapping protein cargo. All exosomal cdEVs were particularly enriched for proteins involved in RNA splicing and nuclear export, and showed distinctive rRNA methylation patterns compared to ssEVs. Overall, this work reveals quantitative and qualitative differences between EVs from steady-state and different regulated cell death conditions.

Abstract

Formation of extracellular vesicles (EVs) has emerged as a novel paradigm in cell-to-cell communication in health and disease. EVs are notably produced during cell death but it had remained unclear whether different modalities of regulated cell death (RCD) influence the biogenesis and composition of EVs. To this end, we performed a comparative analysis of steady-state (ssEVs) and cell death-associated EVs (cdEVs) following TNF-induced necroptosis (necEVs), anti-Fas-induced apoptosis (apoEVs), and ML162-induced ferroptosis (ferEVs) using the same cell line. For each RCD condition, we determined the biophysical and biochemical characteristics of the cell death-associated EVs (cdEVs), the protein cargo, and the presence of methylated ribosomal RNA. We found that the global protein content of all cdEVs was increased compared to steady-state EVs. Qualitatively, the isolated exosomal ssEVs and cdEVs, contained a largely overlapping protein cargo including some quantitative differences in particular proteins. All cdEVs were enriched for proteins involved in RNA splicing and nuclear export, and showed distinctive rRNA methylation patterns compared to ssEVs. Interestingly, necEVs and apoEVs, but strikingly not ferEVs, showed enrichment of proteins involved in ribosome biogenesis. Altogether, our work documents quantitative and qualitative differences between ssEVs and cdEVs.

1 | INTRODUCTION

Recent focus on cell death-associated extracellular vesicles (cdEV) has revealed their implication in multiple functions. Concerning apoptosis, these functions include the ingestion of apoptotic bodies, which stimulates cell division to maintain stemness and epithelial tissue homeostasis (Brock et al., 2019), the apoptotic exosome-like vesicles and their roles as damage-associated molecular patterns (Ito et al., 2021), and the changed protein profile of small EVs from exosomes and large EVs from the cellular surface after the induction of apoptosis (Ito et al., 2021). With regard to necroptosis, the endosomal sorting complexes required for transport (ESCRT)-III mediated release of MLKL during necroptosis (Ito et al., 2021), and the secretion of specific EVs following necroptosis (Ito et al., 2021). Finally, the ferroptosis-dependent EVs contribute to mesothelial carcinogenesis (Ito et al., 2021).

Apoptotic dying cells may produce different types of vesicles, such as apoptotic bodies, which are large membrane-bound structures (500–2000 nm) formed during apoptosis, and exosomes (30–150 nm) released by fusion of multivesicular bodies (MVBs) containing intraluminal vesicles with the plasma membrane, and microvesicles (100–1000 nm) shed by outward blebbing of the plasma membrane (Battistelli & Falcieri, 2020; Kakarla et al., 2020; Meckes & Raab-Traub, 2011; Metzner & Zaruba, 2021; Van Niel et al., 2018). Numerous molecular processes during cell death were identified to contribute to EV biogenesis. Some of these include a component of the ESCRT machinery (Gong et al., 2017; Shlomovitz et al., 2021; Yoon et al., 2017), Rab proteins (Gupta et al., 2022), phosphatidylserine (PS) exposure on the extracellular vesicles during necroptosis (Zargarian et al., 2017), and cytoskeleton reorganization (Park et al., 2018; Tucher et al., 2018; Wickman et al., 2013).

Extracellular vesicles (EVs) are now recognized as playing crucial roles in transferring messages between cells (Mir & Goettsch, 2020; van Niel et al., 2022). The horizontal transfer of information carried out by EVs lies in their intraluminal content (Mir & Goettsch, 2020) comprised of diverse proteins and nucleic acids. The protein composition of cell death EVs (cdEVs) such as apoptotic EVs (apoEVs) (Tucher et al., 2018) and necroptotic EVs (necEVs) (Gupta et al., 2022; Shlomovitz et al., 2021), and heat-shock-derived EVs (Y. Li et al., 2020) has been reported. Despite these recent advances, a systematic comparison of the composition of EVs produced by cells undergoing different regulated cell death (RCD) modalities has not been possible because of the different methodologies used to isolate them, and of the diverse cell types used.

In recent years, the hypothesis that ribosomes are not all produced equally and that compositionally different ribosomes might have different translational outputs has become more and more explored (Genuth & Barna, 2018a). The ribosomal RNA (rRNA) is extensively modified, with one of the most common modifications being sugar 2′-O-methylation (Sharma & Lafontaine, 2015). The current view is that differential rRNA methylation might serve regulatory roles during normal and disease processes by rewiring translation. In particular, differences in rRNA 2′-O-methylation profiles have been associated with cell fate decision pathways, including cell differentiation (van den Akker et al., 2022), tumorigenesis (Marcel et al., 2013; Sharma et al., 2017), and embryonic development (Delhermite et al., 2022; Hebras et al., 2020). Whether exosomal EVs produced under steady-state or cell death conditions contain differentially modified ribosomal RNAs, that could display biomarker potential, has not been explored.

Here we performed a comparative study to systematically determine the proteomic content of particular cdEVs produced by cells undergoing different RCD modalities, aiming to define possible signatures. We induced cell death in a single cell line and isolated EVs for downstream analysis. We compared the physical and biochemical characteristics, and the protein and methylated rRNA cargos of EVs produced during steady-state (ssEVs), TNF-induced necroptosis (necEVs), anti-Fas-induced apoptosis (apoEVs), and ML162-induced ferroptosis (ferEVs). The number of cdEVs released in each RCD modality was always increased compared to steady-state. The overall protein content increased in all RCD conditions, and these cdEVs shared a similar proteomic cargo. The overlap between apoEVs, necEVs and ferEVs consisted of an enrichment in spliceosomal components and nuclear export factors and a distinct rRNA methylation pattern in cdEVs compared to ssEVs. Furthermore, apoEVs and necEVs were enriched in proteins important for ribosome biogenesis, while this was not the case for ferEVs. Altogether, our work reveal important quantitative and qualitative differences between steady-state and distinct cell death EVs.

2 | METHODS

2.1 | Cell culture, reagents, and antibodies

L929sAhFas cells, previously described (Vercammen, Brouckaert, et al., 1998) and further referred to here as L929, were cultured at 37°C under 5% CO_2 in Dulbecco's Modified Eagle Medium (DMEM) supplemented with 10% Fetal Bovine Serum (FBS,

qualified, heat-inactivated, EU-approved, South America Origin), Na-Pyruvate (400 mM), and 2 mM L-Glutamine (Gibco, Thermo Fisher Scientific). Cells were regularly tested against mycoplasma contamination. Recombinant mouse TNFα (TNF) was produced at the VIB Protein Core facility (http://proteincore.sites.vib.be/en). TNF was used at 120 pg/mL. Anti-Fas (hFasL, human, activating, clone CH11, #05-201, Upstate) was used at 70 ng/mL. ML162 (Aobious, Gloucester, MA) was used at 20 μM. The following antibodies were used for immunoblot: Alix (ab76608, Abcam), TSG101 (C-2, sc-7964, Santa Cruz), CD63 (EPR21151, ab217345, Abcam), CD81 (EPR4244, ab109201, Abcam & D5O2Q, 10037, Cell Signalling), Flotillin-1 (EPR6041, ab133497, Abcam), Histone H3b (D1H2, Cell Signalling), Calnexin (610523, BD Biosciences), Calreticulin (EPR3924, ab92516, Abcam), Bcl-2-HRP (C-2, sc-7382, Santa Cruz), LAMP1 (L1418, Sigma-Aldrich), phospho-RIPK3 (E7S1R, 91702S, Cell Signalling), RIPK3 (2283, ProSci Incorporated), phospho-MLKL (D6E3G, 37333S, Cell Signalling), MLKL (3H1, MABC604, Millipore), cleaved Caspase-8 (9429, Cell Signalling), Caspase-3 (9662, Cell Signalling), Caspase-7 (9492, Cell Signalling), PARP (46D11, 9532S, Cell Signalling) and cleaved PARP (9544S, Cell Signalling). HRP-conjugated secondary antibodies were anti-rabbit IgG, anti-mouse IgG, or anti-rat IgG (GE Healthcare, NA934, NA931, NA935, respectively, 1:5000). All antibodies were applied at 1/1000 of the stock solution proposed by the customer except for CD81 (1/500).

2.2 | Protein staining

An identical volume from the different fractions obtained following size exclusion chromatography (SEC) purification was loaded on Bolt 4%–12% Bis-Tris Plus Gels, 15-wells (Life Technologies), and submitted to electrophoresis. Next, the gels were incubated for 30–60 min at room temperature in Coomassie Blue G-250 solution prepared in 50% methanol and 10% acetic acid. After repeated rinsing with water, gels were stained with 40% methanol/10% acetic acid and renewed until the expected staining became visible. Finally, gels were rinsed with water and imaged.

2.3 | Western blot and immunoblotting

For total cell lysates, after indicated stimulation, L929 cells at around 80% confluence at the time of treatment were washed twice in ice-cold PBS and harvested by scraping using ice-cold RIPA lysis buffer (50 mM Tris-HCl, pH 7.5; 150 mM NaCl; 1 mM EDTA; 0.5% sodium deoxycholate; 1% Triton X-100 and 0.1% SDS) freshly supplemented with EDTA-free Complete protease inhibitor cocktail tablets (no. 11873580001, Roche Diagnostics Belgium) and phosphatase inhibitor cocktail tablets (PhosSTOP, no. 04906837001, Roche Diagnostics Belgium). For EV-associated protein immunoblotting, 1 or 10 μg protein equivalent of EVs as determined by Qubit Protein Assay Kit (see below) were taken for each condition and mixed with laemmli buffer containing β-mercaptoethanol. Samples were then boiled for 10 min and subsequently put on ice. Extracted proteins were separated on in-house or Bolt 4%–12% Bis-Tris Plus Gels, 15-wells (Life Technologies), and then transferred onto nitrocellulose membranes (Schleicher & Schuell and PerkinElmer). Membranes were blocked using TBS with 0.05% Tween20 (TBS-T) containing 5% non-fat dry milk. SuperSignal West Atto Ultimate Sensitivity Substrate HRP Chemiluminescence Detection Reagents (ThermoFisher) were used for detection. Precision Plus Protein Kaleidoscope (BioRad) and PageRuler Plus Prestained Protein Ladder (26619, Thermo Fisher Scientific) were used as molecular weight ladders. The membranes were reprobed after incubation in Restore PLUS Western Blot Stripping Buffer (46430, Thermo Fisher Scientific).

2.4 | Preparation of conditioned culture medium (CCM) and EV purification

Two days before the experiment, cells were seeded in 4 × T885 flasks. Before stimulation, cells were rinsed twice with PBS and once with OptiMEM. Cells were covered with 37°C prewarmed 100 ml of OptiMEM per T885 flask. Conditioned medium from L929 cells stimulated (for apoptosis with anti-Fas 70 ng/mL, for necroptosis with TNF at 120 pg/mL, and for ferroptosis with ML162 at 20 μM) or not was collected after 8 h of incubation at 37°C and 5% CO$_2$. To remove the large debris, the CCM was centrifuged twice, at 300 g for 5 min at 4°C and then at 3.000 g for 10 min at 4°C. It was then filtered through a 0.45 μm filter and concentrated to 5 mL (80× concentrated) using a Centricon Plus-70 Centrifugal Filter Unit with Ultracel-PL membrane of 10 kDa cutoff (UFC701008, Amicon). The sample was then kept on ice, and EVs were immediately separated by gel filtration using the qEV-10 columns (qEV10/70 nm SEC columns; Izon Science) according to the manufacturer's instructions. One column was used per condition. Briefly, columns were brought to room temperature, rinsed, and equilibrated with 100 ml PBS. Then the sample was applied, and after discarding the void volume (20 mL), 5 mL fractions were collected. Aliquots of 200 μL of each fraction were kept for further analysis. The fractions 2, 3, and 4 (15 mL)—corresponding to the fractions having the highest number of particles and lower free protein content—were pooled together in a 16.8 mL open-top polyallomer tube (337984, Beckman Coulter). Samples were centrifuged for 3 h at 100.000 g and 4°C (SW 32.1 Ti rotor, Beckman Coulter). The resulting pellet was

resuspended in 200–300 μL PBS and stored aliquoted at $-80°$C. The number of particles was then assessed using a ZetaViewer, and samples were further analyzed.

2.5 | Mass spectrometry: Amphipol-aided protein precipitation

A total of 16 samples were prepared for LC-MS/MS analysis (4 independent experiments each time 4 conditions: untreated (steady-state), necroptosis, apoptosis, ferroptosis—UNAF). First, EV preparations were lysed by the addition of Amphipol A8−35 (APols, Anatrace, cat. No. A835) to a final concentration of 1 mg/mL in phosphate-buffered saline (PBS), vortexed and incubated for 30 min on ice. Next, samples were homogenized by sonication on a Diagenode Bioruptor Plus instrument using the following settings: high-intensity power output, 10 cycles of 30 sec ON/30 sec OFF pulses, $+4°$C water bath. Then, proteins were reduced by adding 15 mM dithiothreitol (DTT) and incubation for 30 min at $55°$C and then alkylated by adding 30 mM iodoacetamide for 15 min at room temperature (RT) in the dark. Next, samples were acidified with 10% formic acid to pH 3 and centrifuged for 10 min at 15,000 g and RT. The resulting protein-containing pellets were washed with 0.1% trifluoroacetic acid (TFA) and re-dissolved in 50 μL 50 mM triethylammonium bicarbonate (TEAB). Then, proteins were digested with 0.1 μg lysyl endopeptidase (Wako) for 4 h at $37°$C, followed by overnight digestion with 0.1 μg trypsin (Promega) at $37°$C. Next, samples were acidified with TFA to a final concentration of 1% (pH < 3), incubated for 15 min on ice, centrifuged for 10 min at 20,000 g, and RT to pellet the precipitated Amphipol A8-35. The peptide-containing supernatant was transferred to new tubes, dried under vacuum, and stored at $-20°$C.

2.6 | Mass spectrometry: Tandem mass tag (TMT) labelling

TMTproTM 16-plex labels (0.5 mg, Thermo Fisher Scientific) were equilibrated to RT immediately before use and dissolved in 25 μL anhydrous acetonitrile (ACN). The dried peptides were resuspended in 20 μL 100 mM TEAB (pH 8.5) and labelled for 1 h at RT using 0.1 mg (5 μL) of TMTProTM label steady-state (SS) aka untreated (Unt) replicates labelled 126C, 128C, 130C and 132C; Necroptosis (Nec) replicates labelled 127N, 129N, 131 and 133N; Apoptosis (Apo) replicates labelled 127C, 129C, 131C, 133C; Ferroptosis (Fer) replicates labelled 128N, 130N, 132N, 134N). The reaction was quenched for 15 min at RT with the addition of 1 μL 5% hydroxylamine. The 16 labelled samples were combined, dried by vacuum centrifugation, re-dissolved in 100 μL 0.1% TFA and desalted on a reversed-phase (RP) C18 OMIX tip (Agilent). The tip was first washed three times with 100 μL pre-wash buffer (0.1% TFA in water/ ACN (20:80, v/v)) and pre-equilibrated five times with 100 μL of wash buffer (0.1% TFA in water) before the sample was loaded on the tip. After peptide binding, the tip was washed three times with 100 μL of wash buffer, and peptides were eluted twice with 100 μL elution buffer (0.1% TFA in water/ACN (40:60, v/v)). The combined elutions were dried in a vacuum concentrator.

2.7 | Mass spectrometry: HPLC fractionation

Vacuum-dried peptides were re-dissolved in 100 μL "solvent A" (0.1% TFA in water/acetonitrile (ACN) (98:2, v/v)), and 95 μL was injected for fractionation by RP-HPLC (Agilent series 1200) connected to a Probot fractionator (LC Packings). Peptides were first loaded in "solvent A" on a 4 cm pre-column (made in-house, 250 μm internal diameter (ID), 5 μm C18 beads, Dr. Maisch) for 10 min at 25 μL/min and then separated on a 15 cm analytical column (made in-house, 250 μm ID, 3 μm C18 beads, Dr. Maisch). Elution was done using a linear gradient from "100% RP-HPLC solvent A" (10 mM ammonium acetate (pH 5.5) in water/ACN (98:2, v/v)) to "100% RP-HPLC solvent B" (70% ACN, 10 mM ammonium acetate (pH 5.5)) in 100 min at a constant flow rate of 3 μl/min. Fractions were collected every minute between 20 and 92 min and pooled every 12 min to generate 12 samples for LC-MS/MS analysis. All 12 fractions were dried under vacuum in HPLC inserts and stored at $-20°$C until further use.

2.8 | Mass spectrometry: LC-MS/MS analysis

The mass spectrometer was operated in data-dependent mode, automatically switching between MS and MS/MS acquisition for the 16 most abundant ion peaks per MS spectrum. Full-scan MS spectra (375-1500 m/z) were acquired at a resolution of 60,000 in the Orbitrap analyzer after accumulation to a target value of 3,000,000. The 16 most intense ions above a threshold value of 15,000 were isolated with a width of 1.5 m/z for fragmentation at a normalized collision energy of 30% after filling the trap at a target value of 100,000 for a maximum of 80 ms. MS/MS spectra (200-2000 m/z) were acquired at a resolution of 15,000 in the Orbitrap analyzer.

The fractionated peptides were re-dissolved in 20 μL "solvent A," and 12.5 μL of each fraction was injected LC-MS/MS analysis on an Ultimate 3000 RSLCnano system in-line connected to a Q Exactive HF mass spectrometer (Thermo Scientific). Trapping was performed at 10 μL/min for 4 min in loading solvent A on a 20 mm trapping column (made in-house, 100 μm internal diameter (ID), 5 μm beads, C18 Reprosil-HD, Dr. Maisch, Germany). Peptides were separated on a 250 mm Waters nanoEase M/Z HSS T3 Column, 100Å, 1.8 μm, 75 μm inner diameter (Waters Corporation), kept at a constant temperature of 45°C. Peptides were eluted by a non-linear gradient starting at 5% "MS solvent B" reaching 33% "MS solvent B" (0.1% formic acid (FA) in water/acetonitrile (2:8, v/v)) in 80 min, 55% "MS solvent" B (0.1% FA in water/acetonitrile (2:8, v/v)) in 104 min, 99% "MS solvent B" in 107 min followed by a 10-min wash at 99% "MS solvent B" and re-equilibration with MS solvent A (0.1% FA in water). The mass spectrometer was operated in data-dependent mode, automatically switching between MS and MS/MS acquisition for the 16 most abundant ion peaks per MS spectrum. Full-scan MS spectra (350-1500 m/z) were acquired at a resolution of 120,000 in the Orbitrap analyzer after accumulation to a target value of 3,000,000. The 16 most intense ions above a threshold value of 15,000 were isolated with a width of 0.7 m/z for fragmentation at a normalized collision energy of 32% after filling the trap at a target value of 20,000 for a maximum of 120 ms. MS/MS spectra (with a fixed first mass of 110 m/z) were acquired at a resolution of 60,000 in the Orbitrap analyzer.

2.9 | Mass spectrometry: Data analysis

LC-MS/MS runs of all 16 samples were searched together using the MaxQuant algorithm (version 1.6.2.6) with mainly default search settings, including a false discovery rate set at 1% on peptide and protein level (PSM). MS2-based quantification using TMTPro16plex labels was chosen as the quantification method. Spectra were searched against the mouse protein sequences in the Swiss-Prot database (database release version of 2021_01), containing 21,989 sequences (www.uniprot.org). The mass tolerance for precursor and fragment ions was set to 4.5 and 20 ppm, respectively, during the main search. Enzyme specificity was set to the C-terminal of arginine and lysine, allowing cleavage at Arg/Lys-Pro bonds with a maximum of two missed cleavages. Variable modifications were set to oxidation of methionine residues and acetylation of protein N-termini, whereas carbamidomethylation of cysteine residues was set as a fixed modification. In order to reduce the number of spectra that suffer from co-fragmentation, the precursor ion fraction (PIF) option was set to 75%. Only proteins with at least one unique or razor peptide were retained, leading to identifying 5261 proteins. MS2-based quantification using TMTpro labels was chosen as the quantification method, and a minimum ratio count of 2 unique peptides was required for quantification. Further data analysis of the shotgun results was performed with an in-house R script, using the protein groups output table from MaxQuant. Reverse database hits were removed, TMT intensities were log2 transformed, and replicate samples were grouped. Proteins with less than three valid values in at least one group were removed, and missing values were imputed from a normal distribution centered around the detection limit (package DEP)(Zhang et al., 2018), leading to a list of 4,984 quantified proteins in the experiment, used for further data analysis. Among these 4984 quantified proteins, 89 were determined as contaminants, and two were not linked to a known gene. Among the remaining 4893 quantified proteins, 4367 were identified as individual proteins and 526 as a protein group.

2.10 | Mass spectrometry: Pairwise analysis

To compare protein abundance between pairs of sample groups (Nec vs. SS Apo vs. SS, Fer vs. SS), statistical testing for differences between two group means was performed using the package limma (Ritchie et al., 2015). The complete list of quantified proteins is presented in Table S1. Statistical significance for differential regulation was set to a false discovery rate (FDR) < 0.05 (-log10 > 1.301) and a variable fold change of FC $\geq$ 1.5 (|log2FC| $\geq$ 0.585) for the 'relaxed' threshold, and FC $\geq$ 4 (|log2FC| $\geq$ 2) for the 'stringent' threshold (referred as down+/up+ or down++/up++, respectively, in Table S1).

2.11 | Mass spectrometry: Multigroup analysis

To compare protein abundance between sample groups (SS vs. Nec vs. Apo vs. Fer), statistical testing for differences between group means was performed using the package limma (Ritchie et al., 2015). Statistical significance for differential regulation was set to a false discovery rate (FDR) of 0.05. In addition, Z-scored LFQ intensities from significantly regulated proteins were plotted in a heatmap after non-supervised hierarchical clustering.

2.12 | Mass spectrometry: Gene ontology (GO) analysis

Two sets of differentially abundant proteins were used for functional characterization. The first set was obtained using the parameter thresholds of adjusted p-value ≤ 0.05 and $|Log2FC| \geq 2$ (4×) (stringent analysis). For the second set, parameter thresholds of adjusted p-value ≤ 0.05 and $|Log2FC| \geq 0.585$ (1.5×) were used (low stringency analysis). To characterize the significantly up and downregulated proteins in cell death conditions versus the steady-state or untreated condition, gene ontology (GO) enrichment analysis was performed using the enrichGO function of the R package clusterProfiler (T. Wu et al., 2021). The p and q value cutoffs were set to 0.01 and 0.05, respectively. Beforehand, proteins were grouped in upregulated and downregulated sets. Then, analysis was done separately for each GO type (Biological Process, Molecular Function, and Cellular Component). We only considered the Biological Process for interpretation, as this was the most informative for our experimental dataset. Finally, summarization of the enriched GO-terms was performed using the web-based GO-terms classification counter CateGOrizer (Hu et al., 2008) and the generic GO Slims classification (GO_Slim2, with root classes removed, from generic GO-subset: http://geneontology.org/docs/download-ontology/). The cateGOrizer tool is available here: https://www.animalgenome.org/tools/catego/.

2.13 | Mass spectrometry: Comparison analysis

The list of comparisons and Venn diagrams were generated using 'Multiple List Comparator' from molbiotools (https://molbiotools.com/listcompare.php) against the exosome proteome databases from Exocarta (970 proteins, #5, release date 29th July 2015, www.exocarta.org) (Keerthikumar et al., 2016; Mathivanan et al., 2012) and Vesiclepedia (4,513 proteins, ver. 4.1, 15th August 2018, www.microvesicles.org) (Kalra et al., 2012; Pathan et al., 2019), and their respective TOP100 proteins. Each dataset was selected for *mus musculus*, and duplicates were removed. In order to have the same identifier to compare, our samples list and the two databases identifier were converted to their official gene symbol for *mus musculus* using the DAVID ID conversion tool (https://david.ncifcrf.gov/conversion.jsp, 2021 Update, NIAID/NIH) (Huang et al., 2009a, 2009b). Lists of converted proteins from both databases are presented in Table S2. Among the 4895 identified proteins, the comparison was performed on the 4396 identified individual proteins, including or not the 526 identified protein groups, depending on the analysis. The individual protein IDs were converted to 4382 official gene symbols; 5 uniprotIDs referred to more than one official gene symbol and thus were used for the comparison. When protein groups were included, their different identifiers were individualized into 1,401 individual protein IDs and converted into 1375 official gene symbols; 7 individual IDs were not linked to an official gene symbol, and 19 uniprotIDs were in duplicate. When a comparison with the group protein was performed, a match between the target database with at least one ID from each individual group was considered a match.

2.14 | RiboMethSeq analysis: Library preparation and bioinformatics

The RiboMethSeq libraries were prepared as described (Marchand et al., 2017). Briefly, total RNA was extracted from purified EVs using the TRI reagent (ThermoFisher, AM9738), according to the manufacturer's instructions and subjected to fragmentation in mild alkaline conditions as described (Marchand et al., 2017). Briefly, RNA was hydrolyzed in bicarbonate buffer and the reaction was stopped by ethanol precipitation. The resulting fragments were then end-repaired and converted into an Illumina library using the NEBNext Small RNA Library Prep kit (Bioke, E7300S) and sequenced at the ULB brightcore facility.

The MethScore was calculated as described in Marchand et al. (2016). Shortly, the score of the nucleotide is the number of reads for that position normalized using the average read number and the standard deviation of the 6 neighbouring residues on either side. Reads were aligned using bowtie2 to reference sequences NR_003279.1 (18S), NR_003280.2 (5.8S), and NR_003279.1 (28S). Clustering was done using Euclidean distances in "R." All RiboMethSeq were performed in duplicate (independent biological samples) on RNA from purified EVs (Figure 4) and matching total RNA of the corresponding producing cells, coined cell body (Figure S6).

2.15 | Cell death measurement

To determine the effect of OptiMEM on the viability and the necroptosis kinetic, cells were seeded on 24-well dishes ibiTreat (Ibidi) to reach 60%–80% confluence at the time of the experiment. On the day of the experiment, to track live and dead cells, Hoechst 33342 (1 μM, ThermoFisher Scientist) and DRAQ7 (1 μM, Biostatus) were added to the pretreatment solution 1 h prior to treatment triggering RCD (for apoptosis with anti-Fas 70 ng/mL, for necroptosis with TNF at 120 pg/mL, and for ferroptosis with ML162 at 20 μM) or not. Cells were then placed inside the microscope stage chamber under controlled temperature, CO_2, and

humidity (top stage incubator, Okolab) 1 h before starting cellular imaging to equilibrate. Wide-field images were captured with a Nikon TiE inverted microscope with a 20X/0.5NA objective and a DS-Qi2 CMOS camera (Nikon). Cell death was determined by monitoring Hoechst and PI fluorescence intensity using video-microscopy with excitation filters 395/25 and 575/25 and emission filters 440/40 and 632/60, respectively. Lumencor provided excitation filters, and all dichroic mirrors and emission filters were obtained from Chroma Technology. An automated emission filter wheel Lambda 10-B Smart Shutter (Sutter Instrument) was used. Quantification was performed using CellProfiler 3.0 (McQuin et al., 2018).

To determine the cell death level during EV production for all 4 experimental conditions, an extra T175 flask/condition was seeded and subjected to a similar procedure as the T885 flasks but adjusted for cell number to reach similar confluency as in T885 (see EV purification subsection). Upon CCM harvesting, cells were detached with Accutase from the T175 flasks simultaneously. Supernatants from T175 flasks were then combined with the detached cells and spun down 500 g for 10 min. Pellets containing dead and living cells were resuspended in DMEM containing 3 μM of DRAQ7 (Biostatus) and processed by Flow Cytometry. The gating strategy was set using a mix of dead and live cells and unstained controls. A minimum of 10,000 gated events were measured per condition. Data were further analyzed using FlowJo (BD).

2.16 | Electron microscopy: Negative staining of cell death EVs

Visualization of purified EVs was performed by EM negative staining. Briefly, formvar/carbon-coated 200-mesh grids treated by glow discharge treatment during 1 min and 20 μL of the sample were adsorbed onto the grids for 1 min at room temperature. Subsequently, grids were washed five times in Milli-Q water droplets, stained with 1% uranyl acetate for 10 sec, and air-dried for 24 h before imaging. Samples were viewed with a JEM 1400plus transmission electron microscope (JEOL, Tokyo, Japan) operating at 80 kV.

2.17 | Protein analysis

Protein concentration of total cell lysate and EVs were measured using Qubit Protein Assay Kit and Qubit 4 (ThermoFisher), following the manufacturer's instructions. Measurements were performed in triplicate, and the mean was calculated and represented for each independent experiment.

2.18 | Nanoparticle tracking analysis (NTA)

To determine the number of particles in EV enriched fractions, a ZetaView analysis was performed. Before the measurement, samples were diluted in PBS until their particle concentration was within the instrument's optimal concentration range (100−400 particles/frame). Next, samples were injected into the ZetaView PMX-120 instrument (Particle Metrix, Germany) equipped with a 520 nm laser. Two cycles of each 11 positions were performed for each measurement, capturing 30 frames per position. All settings were kept constant (focus: autofocus; camera sensitivity: 82; shutter: 100; scattering intensity: detected automatically; temperature: 23°C; video length: high). Videos were analyzed by the ZetaView software version 8.04.02 SP2 to determine the concentration and size of measured particles. NTA post-acquisition settings were optimized and kept constant between samples (min size: 10; max size: 1000; min bright: 30; trace length: 15). Absolute numbers were recorded and back-calculated using the dilution factor. Before analysis, the ZetaView system was calibrated with polystyrene latex microbeads at 100 nm (Particle Metrix).

2.19 | EV surface marker analysis

EVs were quantified using single-particle interferometric reflectance imaging sensing (Exoview instrument, Nanoview Biosciences) and fluorescently labeled antibodies targeting CD81 and CD63. Briefly, fresh CCM was diluted at 1:10 in incubation buffer. A volume of 35 μL was put on the ExoView Tetraspanin Chip (EV-TETRA-M2) and placed in a 24-well plate for 16 h at room temperature. Then, chips were washed three times for 3 min on an orbital shaker with the wash solution. Next, chips were incubated at room temperature for 1 h in 250 μL of labelling solution. Antibodies (anti-CD81 (Eat-2) CF®555 and anti-CD63 (NBG-2) CF®647) were diluted 1:5000 in incubation solution containing 2% BSA. Chips were then washed once in incubation solution, three times in wash solution, followed by rinsing in Milli-Q water, and finally dried. All chip manipulations avoided drying the chip during washing steps to prevent denaturation and increase specificity. Chips were imaged with the ExoView R100 reader using the ExoScan 2.5.5 acquisition software, and data were analyzed using ExoViewer 3.0 with sizing thresholds set to 50 to 200 nm diameter.

2.20 | Material accessibility

All relevant data of our experiment were submitted to the EV-TRACK knowledgebase (van Deun et al., 2017) with the EV-track ID PXD039297. In addition, proteomics data were deposited on the ProteomeXchange Consortium via the PRIDE partner repository with the ID PXD039297. The RiboMetSeq data have been deposited in NCBI's Gene Expression Omnibus, and is accessible through GEO Series accession number GSE221999.

3 | RESULTS

3.1 | Purification of EVs produced following TNF-induced necroptosis, anti-Fas-induced apoptosis and ML162-induced ferroptosis

Production of EVs is enhanced during different RCD modalities (Brown et al., 2019; Gupta et al., 2022; Ito et al., 2021; Kajiwara et al., 2022; Tucher et al., 2018; Wickman et al., 2013; Yoon et al., 2017). However, neither the amount of EVs nor the EV protein composition has been systematically compared thus far during different RCD in one single cell type. Therefore, we characterized cell death EVs (cdEVs) derived from three RCDs in L929sAhFas (hereafter called L929), a versatile cell line allowing induction of multiple forms of RCD and associated production of EVs. TNF-induced necroptosis EVs (necEVs), anti-Fas-induced apoptosis EVs (apoEVs), and ML162-induced ferroptosis EVs (ferEVs) were compared with EVs released at steady-state (ssEVs) (Figure 1a). For EV production, L929 cells were cultured in serum-free medium for 8 h generating about 50% cell death in all three RCD conditions. The serum-free conditions did not affect viability or cell death kinetics (Figure S1a). After 8 h of incubation, cells were visually inspected (Figure 1b), the CCM was harvested, and the amount of cell death was assessed (Figure 1c). CCM was pre-cleared using centrifugation and 0.45 μm filtration (Figure 1a). Note that owing to the pre-clearing procedure, our study has focused on small EVs (<450 nm diameter). EVs were then purified from the supernatant by SEC. The EV-containing fractions F2-F3-F4 were pooled and subsequently analyzed for particle concentration (Figure S1b), amounts of soluble proteins (Figure S1c-d), and EV markers CD81, Alix, (Figure S1e).

After pooling the three gel filtration fractions (F2-F3-F4), a subsequent ultracentrifugation step was performed (Figure 1a), the pellets were resuspended in PBS, and the EVs were further characterized. The number of cdEVs released in each RCD modality was always increased compare to steady-state, albeit not significantly (Figure 1d). A higher total protein concentration was found in the cdEVs preparation compared to ssEVs (Figure S1f). For all EVs a similar size profile was revealed (Figure 1e), with a mean size of 130–140 nm and a most represented mode size of 100–110 nm diameters (Figure 1e). The latter coincides with the average range of reported sizes of exosomes (30–150 nm) (Battistelli & Falcieri, 2020; Kakarla et al., 2020; Meckes & Raab-Traub, 2011; Metzner & Zaruba, 2021; Van Niel et al., 2018). The transmission electron microscopy revealed heterogeneous vesicular structures ranging in diameter from 50 nm to 300 nm, confirming the NTA data (Figure 1f). The ssEVs and cdEV samples contained the membrane-associated markers involved in biogenesis of exosome formation including TSG101 (member of ESCRT-I complex), Alix (ESCRT-III activator) (Figure 1g), the tetraspanins CD81 and CD63 (Figure 1g-h), the lipid raft-associated protein Flotillin, and the luminal marker histone H3b (Figure 1g) (Larios et al., 2020; McAndrews & Kalluri, 2019). The presence of CD81, CD63 and LAMP1 (Figure 1g-h & S1g), suggests that the exosomes maybe derived from lysosomes or late endosomes (Mathieu et al., 2021). Interestingly, neither calnexin nor calreticulin were detected in any of the EV preparations, even not in cdEVs (Figure 1g-h). This observation questions the use of calnexin and calreticulin as a universal marker for cell death-derived EVs (Tucher et al., 2018). Finally, using single-particle interferometric reflectance imaging with fluorescently labelled antibodies (Figure S1h), we observed an increased level of CD81 and CD63 positive particles (Lamparski et al., 2002) in necroptosis and to a lesser extent in apoptosis. Altogether, our results reveal an increase in exosomal EV production during apoptosis, necroptosis, and ferroptosis, resulting in a higher protein load in total cdEVs compared to ssEV. The cdEVs analyzed showed no noticeable variability in biophysical properties or membrane-associated markers.

3.2 | Systematic analysis of cell death EV proteomes

To investigate EV protein content, cdEVs pellets of four biological repeat experiments of independently purified EVs of all RCD conditions were prepared for proteomic analysis by mass spectrometry (MS). We used the tandem mass tag (TMT) isotopic labelling to enable the protein-wide assessment by liquid chromatography-tandem mass spectrometry (LC-MS/MS) across all 16 samples simultaneously (J. Li et al., 2020). Protein identification and quantification using MaxQuant identified a total of 4895 quantified proteins which were used for further qualitative and quantitative analysis (Figure 2a, Figure S2a). Firstly, a principal component analysis (PCA) revealed clear clustering of the replicates in each condition, demonstrating robustness, with an outspoken segregation between cdEVs and ssEVs (Figure 2b). Moreover, a statistical multigroup analysis revealed 3139 significantly
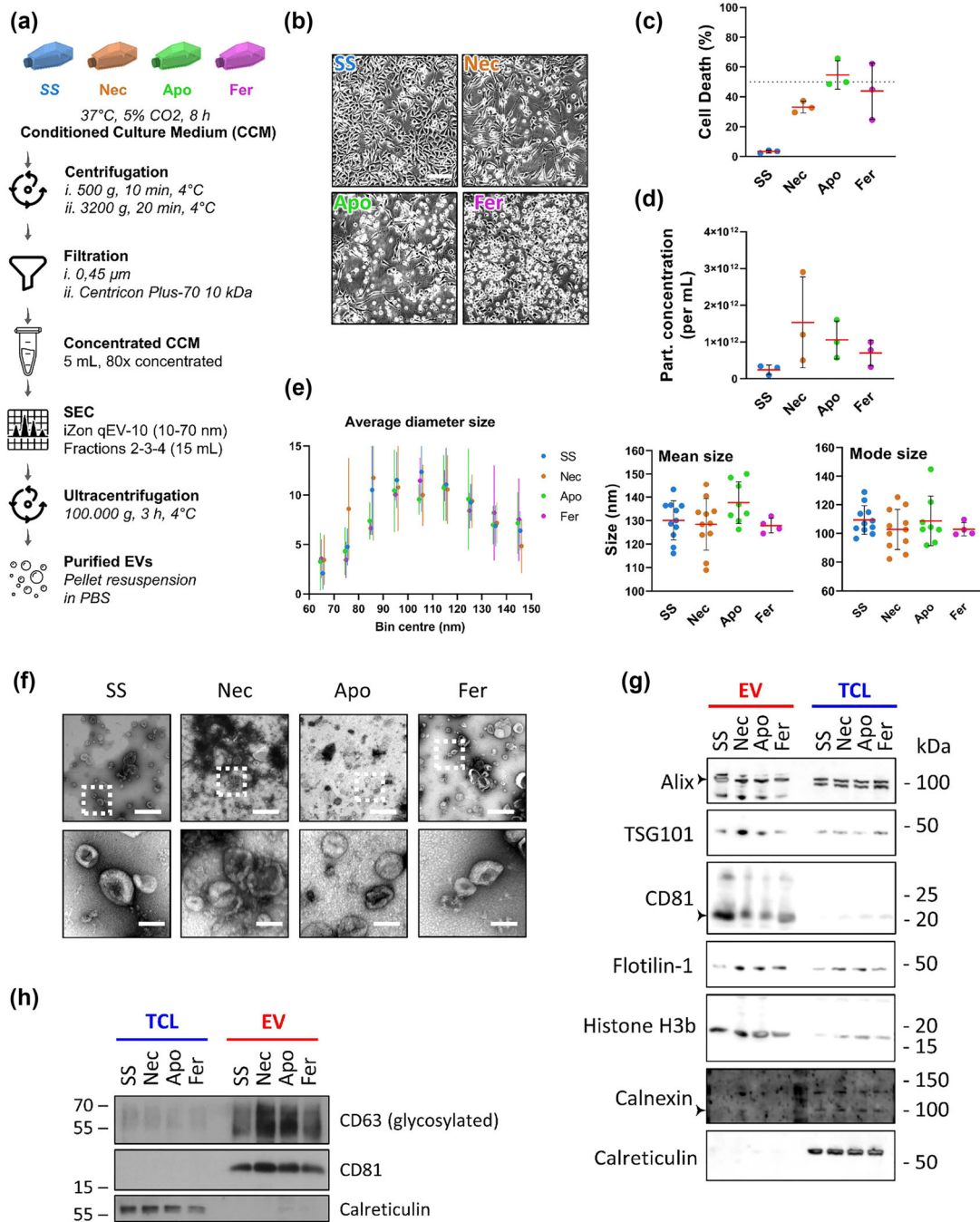
FIGURE 1 EV yield during necroptosis, apoptosis, and ferroptosis. (a) Schematic overview of the experimental procedure for EV production and purification. L929sAhFas cells were left untreated (unt) as steady-state control (ss) or stimulated for necroptosis (nec, stimulated with TNF), apoptosis (apo, stimulated with anti-Fas), or ferroptosis (fer, stimulated with ML162). The drug concentration was adjusted to obtain approximately 50% cell death after 8 h of incubation. The conditioned culture medium (CCM) was harvested for EV purification at that time. Four independent experiments were performed for each condition, serving as biological replicates. (b) After 8 h of treatment, cells were microscopically examined to document the efficacy of cell killing. Scale bar: 100 μm. (c) Cell viability was determined and measured by flow cytometry using DRAQ7. (d-e) The pellet obtained after ultracentrifugation (3 h, 100.000 g, 4°C) was resuspended in PBS. For each replicate particle concentration (panel d), average size distribution, mean and mode size (panel e) were measured by nanoparticle tracking analysis (NTA). No statistical difference was found in panel d. The size distribution represents the average of three replicates. The mean and mode size represent all samples measured for the indicated conditions. (f) Transmission Electron Microscopy (TEM) micrographs of EVs from the conditions indicated. Samples were negatively stained with uranyl acetate. Upper and lower images represent a 15k and 50k magnification, respectively. The lower panel corresponds to a zoom depicted by the dotted square. Representative images and samples were depicted. Scale bar: 500 nm (upper panels) and 100 nm (lower panels). (g-h) Immunoblots were performed on purified EVs and total cell lysate (TCL) and probed for the indicated protein. 1 μg (panel h) or 10 μg (panel g) of protein was loaded per lane. Data represent two (g-h) and three (b-e) independent experiments. SS, steady-state; Nec, necroptosis; Apo, apoptosis; Fer, ferroptosis; CCM, conditioned culture medium; SEC, size exclusion chromatography; TCL, total cell lysate. Data in (c-e) are presented as means ± SD. Statistical analyses were performed using PRISM 9 software (GraphPad). Statistical significance was determined using one way ANOVA with Dunnett's multiple comparison test as a post-hoc test and compared to untreated (SS). $p < 0.1$ tendency, $*p < 0.05$, $**p < 0.01$, $***p < 0.001$, $****p < 0.0001$, ns non-significant.
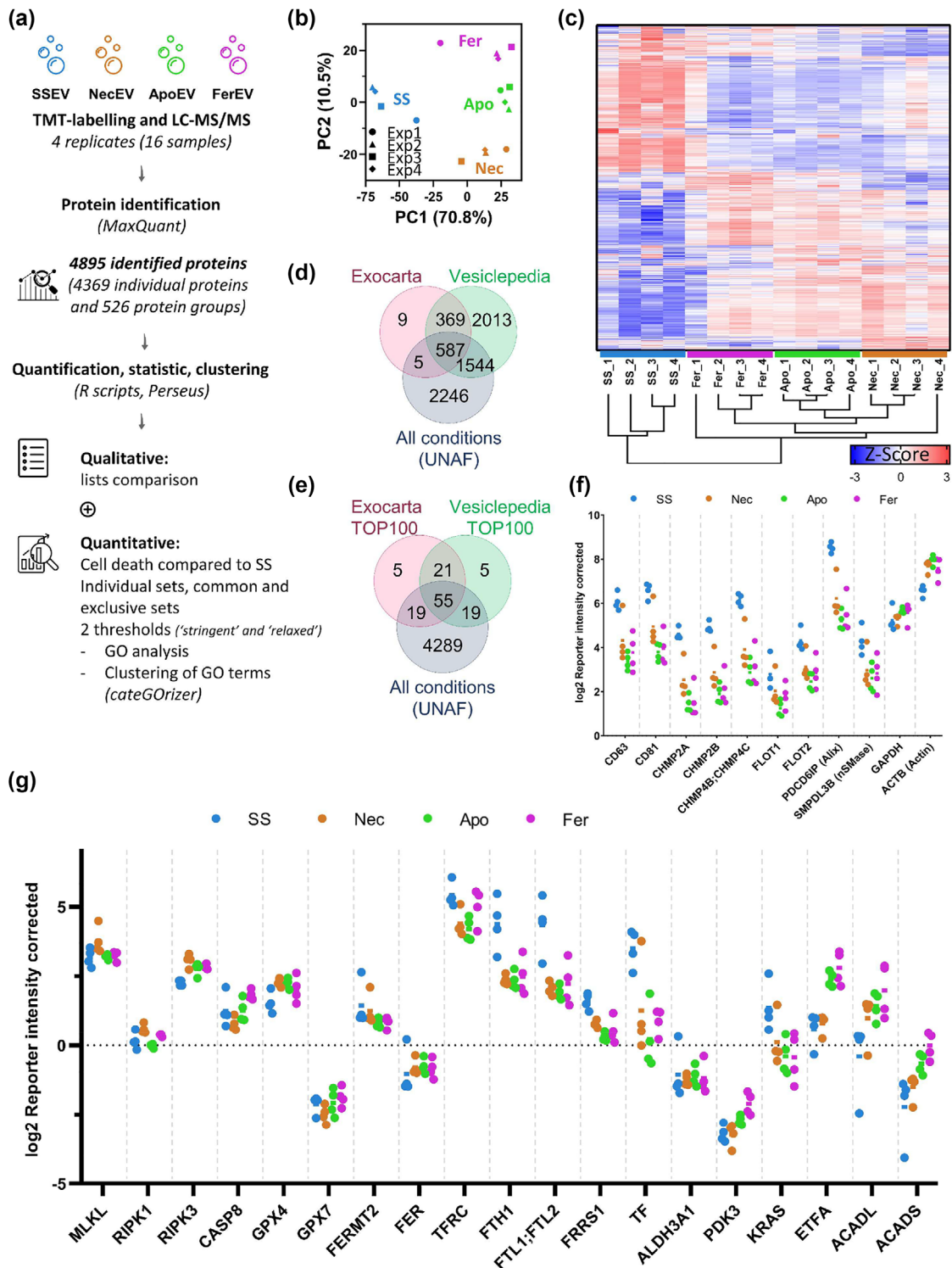
FIGURE 2 Proteome from cdEVs is distinct between cell death and control conditions. (a) Schematic overview of the MS-based proteome analysis. Tandem mass tag (TMT) labelling was performed prior to LC-MS/MS analysis, protein identification by MaxQuant and further qualitative and quantitative analysis. (b) A PCA was performed on the data obtained from each analyzed sample. (c) Heatmap showing 3139 significantly regulated proteins (FDR < 0.05) after non-supervised hierarchical clustering. The colour represents the Z-scored $\log_2$ TMT intensities of each protein in the different samples. (d) Venn diagrams showing the overlap between 4382 proteins identified in this study (proteins with converted gene symbols (Figure S2a) and the murine proteins listed in Exocarta and Vesiclepedia as well as (e) their 100 most abundant proteins (TOP100). (f) Representation of the $\log_2$ TMT values from selected proteins in the different EV subtypes (average and independent experimental data) or (g) related to the different cell death processes. The complete list is available as a table in the supplementary material (Table S2). GO, gene ontology; FDR, false discovery rate; LFQ, label-free quantification. The complete list of proteins is available in Table S2.

regulated proteins (FDR < 0.05) that clustered into two main groups, again separating cdEVs from ssEVs. This analysis highlighted proteins that are up- or down-represented in each class of EVs (ssEV, apoEVs, necEVs, ferEVs) (Figure 2c). The differences in protein abundance were less pronounced when comparing the different cdEV categories between themselves (Figure 2c), arguing for an overall overlap in cdEV protein composition irrespective of the RCD modality. However, there were also quantitative differences in particular proteins between cdEVs, indicating cell death-type specificity.

To quality check the isolation procedure and the proteomics, we compared the ensemble of proteins identified in all conditions with those of the mouse exosome proteome database available from currently published literature on EV content and deposited in Exocarta (Keerthikumar et al., 2016; Mathivanan et al., 2012) and Vesiclepedia (Kalra et al., 2012; Pathan et al., 2019). We found an overlap of 40% with Exocarta and 75% with Vesiclepedia (Table S2), amounting to 592 and 2131 proteins, respectively (Figure 2d). When identified protein groups were included, a total of 2490 items were found in these EV databases (Figure S2b). Protein groups represent the deduced proteins based on the identified peptides following mass spec. In addition, a similar analysis performed using the TOP100 proteins of both databases yielded a 74% recovery rate for individually identified proteins (Figure 2e), and of 81% when protein groups were included (Figure S2b). Importantly, our study contributes an additional 2246 novel proteins to the previously known EV proteome (Figure 2e).

Next, we determined the abundance of classical EV-associated marker proteins, such as CD63, CD81, CHMPs, TSG101, FLOT2 and Alix in steady-state (ssEVs) and RCD conditions (necEVs, apoEVs, ferEVs). Interestingly, in all three RCD conditions these markers were relatively under-represented compared to the steady-state condition (Figure 2f), while this was not the case for the presence of glyceraldehyde dehydrogenase (GAPDH) and β actin (ACTB) as reference proteins in the EVs. This finding indicates that the relatively enriched presence of proteins in the cdEVs compared to steady-state composition may be the result of an adaptive cellular response following cell death induction, during which the classical EV-associated marker proteins remain largely unchanged. The global cargo protein content increased compared to ssEVs (Figure S1f). In contrast to previously reported findings (Gupta et al., 2022; Shlomovitz et al., 2021), we did not really find an increased presence of RIPK3- and MLKL-derived peptides in necEVs compared to the ssEVs, apoEVs and ferEVs. This indicates that the presence of necroptosis pathway associated proteins by itself is not a distinctive marker. The same holds true for presence of caspase-8 as apoptosis marker where no difference was found between all four EVs examined (Figure 2g). For ferEVs and apoEVs, we observed a relative enrichment of several mitochondrial proteins, such as the electron transfer flavoprotein subunit alpha (ETFA) and the short- and long-chain specific acyl-CoA dehydrogenases (ACADS and ACADL); all three involved in β-oxidation of fatty acids, a process upregulated during ferroptosis in breast cancer cells (Panzilius et al., 2019).

In view of the results based on proteomics that reveal non-discriminative presence of necroptotic (RIPK3, MLKL) and apoptotic (caspase-8) cell death proteins in EVs of all conditions, we performed WB analysis to validate the presence and the activation state of these proteins in total cell lysate (TCL) and EVs. The WB results revealed that during TNF-induced cell death the MLKL pore forming protein is phosphorylated (Sun et al., 2012) while no activated initiator caspase-8 (p43, p20) and executioner caspase-3 (p17) and caspase-7 (p20) are present, neither their cleaved substrate PARP (p84) (Figure S2c). These apoptotic parameters are clearly activated during anti-Fas-induced cell death (Figure S2c). This identifies TNF-induced cell death in L929sA cells as purely necroptotic (Duprez et al., 2011). However, during anti-Fas-induced cell death induction phosphorylated MLKL was also detectable both in total cell lysate as well as in EVs, indicating that during large-scale conditions of EV production anti-Fas also engages the necroptotic signalling pathway underlying or parallel with the apoptotic pathway. Interestingly, ML162-induced ferroptosis revealed engagement of the apoptotic pathway as revealed by the presence of activated caspase-8 (only p43, but not p20), cleaved caspase-3/7 (p17/p20) and cleaved PARP (p84) (Figure S2c). Also, the necroptotic pathway seems to be engaged in view of the phosphorylation of MLKL, though no higher molecular weight bands were observed during ferroptosis, in contrast to necroptosis (Figure S2c). This suggests that cellular stress associated with lipid peroxidation in ER, mitochondria and plasma membrane may engage apoptotic and necroptotic signalling pathways. The endoplasmic reticulum (ER) membrane has been identified as a key initiation site of lipid peroxidation during ferroptosis (von Krusenstiern et al., 2023). Indeed, crosstalk between ferroptosis and apoptosis has been reported, but the precise mechanism involved is not clear (P. Wu et al., 2023). In contrast to anti-Fas-derived EVs, no p20 caspase-8 was detected in case of ML162-derived EVs, suggesting an alternative way of caspase-8 activation only resulting in p43 caspase-8 and not in full processing of caspase-8. Altogether, these data show the existence of crosstalk between the RCD pathways (Bedoui et al., 2020). Despite this crosstalk, PCA analysis (Figure 2b) based on EV proteomics of four independent experiments still supported a separate clustering.

3.3 | Cell death EV content is enriched in distinct RNA-related proteins

To assess any putative differences in protein composition in cdEVs, we approached our data set with a different granularity of analysis. We first performed a low stringency pairwise analysis (p-value ≤ 0.05 and $|\log_2 FC| \geq 0.585$, i.e., ≥ 1.5-fold increase or decrease) on the proteomic EV content of each RCD condition versus steady-state as represented by the volcano plots (Figure S3a). For comparison' sake, what we refer to here as 'low stringency analysis' is already more stringent than the published analysis of necroptotic vesicles (p-value ≤ 0.1 and $|\log2FC| \geq 0.1$, i.e., ≥ 1.072 fold increase of decrease) (Gupta et al., 2022; Shlomovitz

et al., 2021). To further assess differences more globally, we also performed a more stringent analysis (p-value ≤ 0.05 and $|\log_2 FC|$ ≥ 2, i.e., ≥ 4-fold increase or decrease) (see next paragraph) (Figure 3a & Table S3).

The Venn diagram of the low stringency analysis illustrates a massive overlap in the increase of protein abundance between all RCD conditions compared to steady-state (Figure S3b). The complete set includes the exclusive, the overlapping (with an other RCD) and shared (between all RCD) changed proteins (increased or decreased), while the exclusive set only contains the non-overlapping and non-shared proteins, unique for a particular RCD modality. A GO-term enrichment analysis was performed, and the GO annotations classified using the web-based GO-terms classification counter CateGOrizer and the generic GO Slims classification (Figure 2a, more information in Methods). Further analysis of the cdEVs content using the low stringent settings were submitted to the GO-terms classification counter and displayed as 'biological process' (Figure S3c). This analysis did not yield exclusive differences between cdEVs. The GO-term enrichment analysis revealed that particular proteins were more abundant in cdEVs than ssEVs, irrespective of RCD, and were involved in RNA-related processes, such as ribosome biogenesis, RNA splicing, RNP complexes, RNA transport, and localization (Figure S3d). A similar analysis of the complete set of RCD conditions versus steady-state confirmed this observation (Figure S4a-c), suggesting an overall enrichment of proteins involved in RNA-related processes in cdEVs. When the exclusively increased protein content was taken into account, we found in the case of necEVs proteins involved in RNA catabolism, clathrin coat assembly, and endocytosis were enriched. In the case of apoEVs, the enrichment of exclusive proteins involved rRNA processing and ribosome biogenesis. Finally, in the case of ferEVs, only a few proteins were exclusively enriched. Those were associated with mitochondrial dicarboxylic acid metabolism, carboxylic and organic acid catabolism (Figure S4d-f).

As indicated above, to assess differences globally, we also analyzed the data set using a stringent threshold (p-value ≤ 0.05 and $|\log_2 FC| \geq 2$, i.e., 4-fold increase or decrease) (Figure 3a). As expected, this yielded a much-reduced list of over- and under-represented proteins in each RCD condition. A high proportion of proteins displaying increased abundance remained shared between the different cdEVs (Figure 3b). The GO-terms classification of the stringent threshold data set reinforced the marked differences between apoptosis and necroptosis associated EV proteome versus the ferroptosis protein EV cargo. Nucleic acid-related metabolism processes emerged strongly in biological processes in both complete and exclusive sets for apoEVs and necEVs cargo (Figure 3c). The enriched proteins of biological processes shared by apoEVs and necEVs include ribosome biogenesis, rRNA metabolic processes, rRNA processes, and (m)RNA catabolic processes, which are not shared by ferEVs (Figure 3d). A detailed breakdown of cdEVs-associated proteome of shared upregulated proteins indicated role in RNA splicing, RNA catabolic processes, mRNA metabolic and catabolic processes (Figure 3e). The common proteins enriched in the EVs of all three RCD processes include RNA splicing, spliceosome, RNA transport and localization, and RNA transport from the nucleus (Figure 3d-e). The GO-term classification on the complete sets showed the highest abundance of proteins involved in ribosome biogenesis and rRNA metabolism in both apoEVs and necEVs content, and of mRNA splicing proteins in ferEVs (Figure S5a-c). When looking at specific enrichment for each RCD condition, besides the ribosome biogenesis and ribosomal components, an apparent dichotomy between cdEVs in specific RNA-related proteins was observed (Figure S5d-f). Indeed, for necEVs, RNA and mRNA catabolism are highly enriched (Figure S5d), while for apoEVs, proteins related to rRNA processing and DNA processes are augmented (Figure S5e), and for ferEVs, fatty acid β-oxidation in mitochondria and tRNA processing (Figure S5f). The latter findings are in agreement with the less stringent analysis described in the above paragraph (Figure S3 and Figure S4).

## 3.4 | Cell death EVs are enriched in differentially methylated ribosomal RNAs

The observation that EVs from cells undergoing cell death are enriched for proteins involved in ribosomal assembly and function, prompted us to investigate whether ribosomal RNA can be detected in EVs and, if so, whether a specific methylation signature might be established. The current view is that differential ribosomal RNA (rRNA) methylation might serve regulatory roles during normal and disease processes by rewiring translation (Gay et al., 2022; Genuth & Barna, 2018b). Differentially modified ribosomes would translate preferentially particular mRNAs, for example, depending on the presence of *cis*-acting elements such as an internal ribosomal entry site. Notably, differences in rRNA 2′-O methylation profiles have been associated with cell fate decision pathways, including cell differentiation (van den Akker et al., 2022), tumorigenesis (Marcel et al., 2013; Sharma et al., 2017), and embryonic development (Delhermite et al., 2022; Hebras et al., 2020), suggesting it could also be playing an essential role in regulation of cell death and associated processes.

Ribosomal RNAs are extensively modified. One of the most common modifications is sugar 2′-O methylation (Sharma & Lafontaine, 2015). We choose a sensitive deep-sequencing-based method to test for the presence of rRNA in purified EVs, and to establish its methylation status systematically. Using RiboMethSeq, we identified all 109 methylated positions expected on mouse rRNA (Figure 4a), implying that rRNA are abundantly present in both ssEVs and cdEVs. The methylation status of each nucleotide is quantitatively expressed by a methylation score ranging from 0 (never identified as being methylated) to 1 (always found to be methylated). Most positions were fully modified (appearing red in the heatmap), while some positions showed variability (Figure 4a and Table S4). Setting a methylation score of 0.65 or below as a threshold value (Sharma et al., 2017),
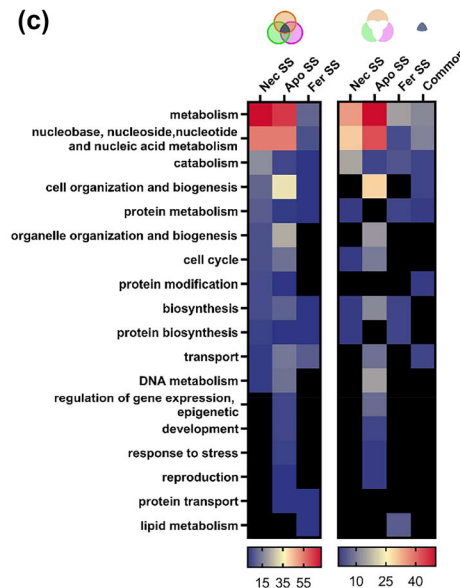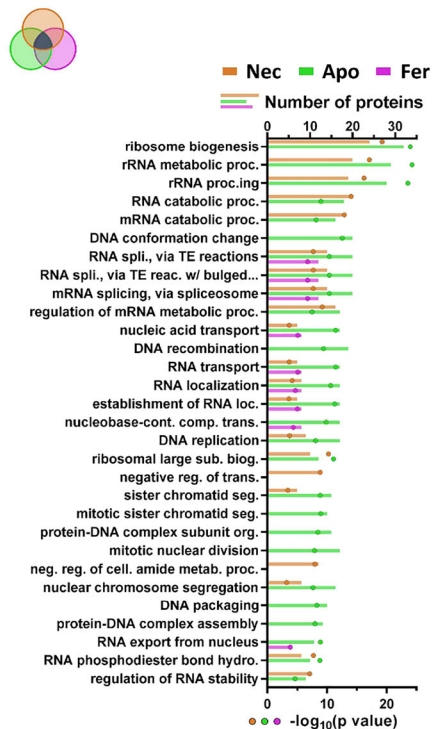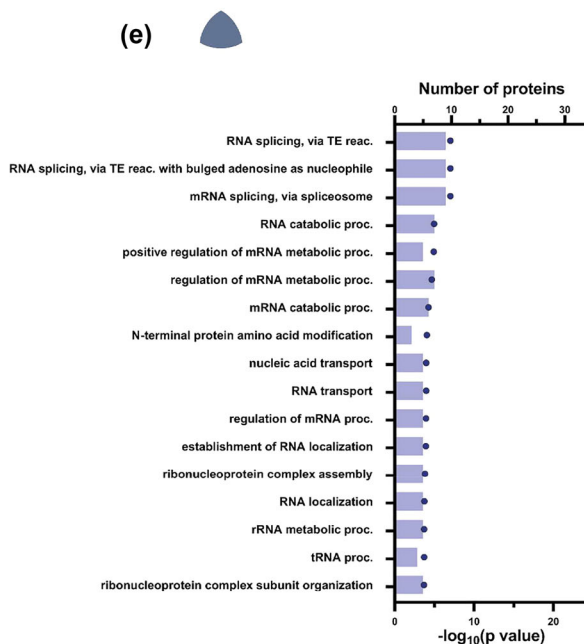
(a) High stringency thresholds
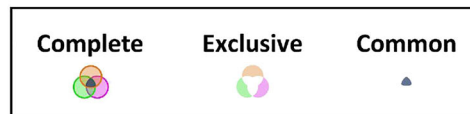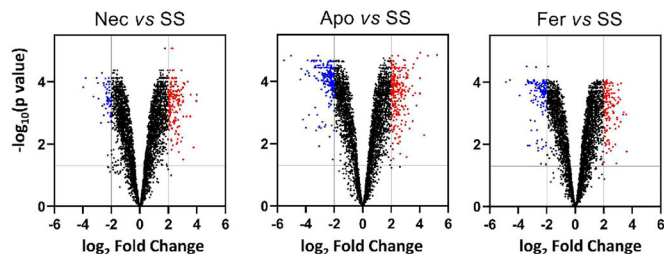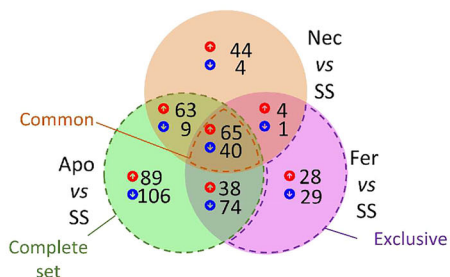
FIGURE 3 High stringency threshold proteomic analysis identifies strong commonalities between different cdEVs. (a) Volcano plot of quantified changes in protein content of each cdEVs compared to ssEVs. The vertical grey lines indicate |log2-fold change (FC)| = 2 (cdEVs relative to ssEVs). The horizontal grey lines indicate p-value = 0.05. The blue and red dots depict the identified proteins in cdEVs that decrease or increase compared to ssEVs, respectively. (b) Venn diagram of the differential abundance of the identified proteins after pairwise comparison. The blue and red arrows represent the number of decreased or increased proteins, respectively. The terminology of the categories used in the GO analysis is depicted in grey. Distinction between "complete set," "exclusive set" and "common set" of proteins is indicated on the Venn-diagram. (c) Based on the upregulated proteins identified, GO-terms were classified using the web-based tool CateGOrizer. The heat map represents the number of proteins identified per class. The analysis was performed on each complete, exclusive, and common set of proteins and classified as biological process (c). The classification was performed using the SLIM table where root terms were removed (SLIM2),

(Continues)

as detailed in the materials and methods. (d) Representation of the enriched GO-terms shared by an increased protein abundance at the intersections between the three cell death conditions obtained by stringent analysis. GO-terms are represented as biological processes (TOP30). The bars represent the number of proteins per GO-term, and the point represents the p-value of the enrichment. (e) Representation of the most enriched GO-terms shared by all three cell death conditions for biological process (TOP30). The bars represent the number of proteins per GO-term, and the circle represents the –log10(p-value) of the enrichment.
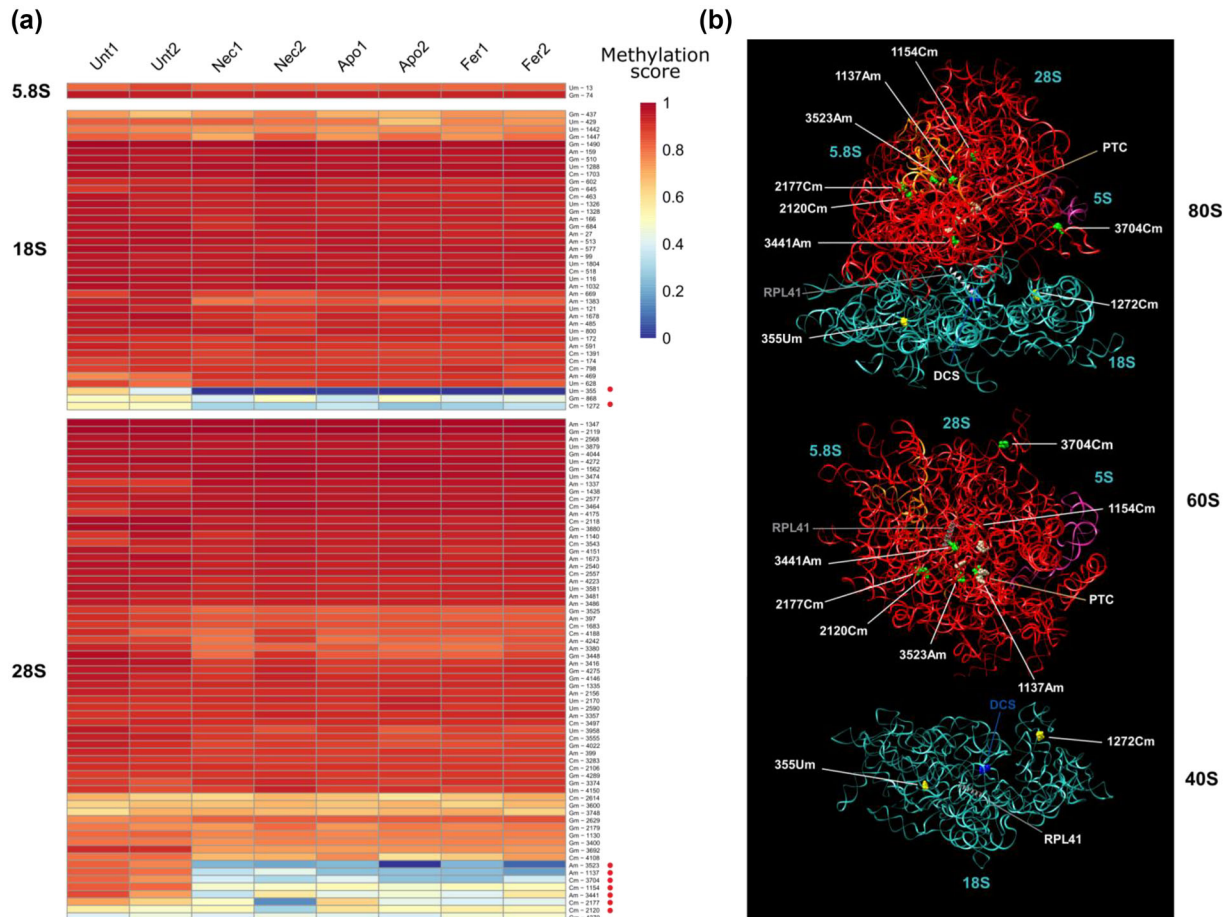

FIGURE 4 Cell death EVs are specifically enriched in differentially methylated ribosomal RNAs. (a) Systematic ribosomal RNA methylation analysis by RiboMethSeq in cells undergoing cell death according to the indicated modality. Each condition was assessed in duplicate. Each raw of the heatmap corresponds to a particular site of 2′-O methylation whose modification level is represented according to the methylation score colour key (a score of 1, displayed in red, corresponding to position modified on all ribosomes analyzed; a score of 0, displayed in blue, corresponding to positions never modified). The modified positions are indicated following the numbering of the rRNA position. Samples were clustered using "R." Positions differentially methylated in cdEVs are highlighted with a red dot. (b) Spatial distribution on the 3-D map of the mouse ribosome of the variable ribose-methylated residues detected in EVs produced by cells undergoing cell death (ribosome model based on PDB 7LS2). Top panel, the 80S ribosome with the small subunit (40S) in cyan, and the large subunit (60S) in red. Differentially modified nucleotides are highlighted. The four ribosomal RNAs (18S in the small subunit, and 5S, 5.8S, and 28S in the large subunit are color-coded). The important functional sites: PTC, peptidyl transferase centre; and DCS, decoding site are indicated. RPL41, is a ribosomal protein that extends from the large subunit into the small subunit forming an inter-subunit bridge acting as a pivot during translation, is indicated for reference. Middle panel, large subunit viewed from the interface. Lower panel, small subunit viewed from the interface.

we were able to identify 15 hypomethylated sites: 12 on the large subunit (LSU) (Am1137, Cm1154, Cm2120, Cm2177, Cm2614, Am3441, Am3523, Gm3600, Cm3704, Cm3748, Cm4108, and Gm4270 – mouse numbering) and 3 on the small subunit (SSU) (Um355, Gm868, and Cm1272) (Figure 4a and Table S4). Of these 15 hypomodified positions, 9 are specific to cell death: SSU-Um355, SSU-Cm1272, LSU-Am1137, LSU-Cm1154, LSU-Cm2120, LSU-Cm2177, LSU-Am3441, LSU-Am3523, and LSU-Cm3704 (annotated with a "red dot" on Figure 4a, using a threshold of 0.65). Importantly, the nine identified cell death-specific positions are diagnostic and may define a novel cell death biomarker for mouse or possibly their equivalent positions on human rRNAs (Table S5). The presence of hypo-modified ribosomal RNAs in cell death EVs suggest they may play a regulatory role in cell death and/or in transmitting cell-to-cell information.

At this stage, we had clearly observed differentially methylated rRNAs in cdEVs. It was unclear if this resulted from random sampling of compositionally different cytoplasm of cells undergoing cell death, or if it was due to a particular enrichment in the vesicles, by a yet to be determined mechanism. To distinguish these possibilities, we repeated the RiboMethSeq analysis, now using total RNA extracted from the matched cells from which the EVs were initially purified (referred to as 'cell body' in Figure S6). A site-to-site comparison of the cell body and exosomal rRNA RiboMethSeq analyses reveals an overall conserved trend in the methylation scores across the two experiments, attesting of robustness (Figure S6 and Table S4). Close inspection of the data further indicates that of the nine positions hypomodified in cdEVs as discussed above, remarkably, seven are specifically enriched in exosomal fractions by comparison to cell body (annotated with a "blue dot" on Figure S6, using a 2-fold change). Finally, it was also interesting to observe that five positions were more modified in control EVs (Unt1 and Unt2) than in control cell body fractions (Figure S6, "green dots", 0.65 threshold). Although not directly relevant to cell death, this reinforces the idea that packaging of modified rRNAs in EVs is not random.

In conclusion, our comparative analysis of ribosomal RNA 2′-O methylation in cells undergoing cell death according to different modalities, and in EVs purified from them, revealed a specific enrichment of differentially modified rRNA in the produced exosomal EVs.

4 | DISCUSSION

The intrinsic connection between cell death and inflammation depends on the release of damage-associated molecular patters (DAMPs), cytokines, and chemokines following plasma membrane permeabilization by mixed lineage kinase-like protein (MLKL) in the case of necroptosis and gasdermin D in pyroptosis (Wallach et al., 2016). Also, ferroptosis leads to plasma membrane permeabilization, massive release of DAMPs (Wiernicki et al., 2022), though this type of regulated necrotic cell death has been shown to have immunosuppressive properties (Kim et al., 2022; Wiernicki et al., 2022). For many years, the field of extracellular vesicles was ignored because such particles were considered as mere debris or cellular waste (Buzas, 2022). Now, EVs are recognized as important modulators of the immune system, including inflammation, antigen presentation, and the development and activation of B and T cells (Buzas, 2022). Considering the intricate relationship between cell death processes and intercellular communication, such as those involved in immune regulation, we wondered whether distinct forms of RCD, including apoptosis, necroptosis, and ferroptosis, could be associated with production of EVs with distinct content and thus differential intercellular effects. Several studies reported on the proteome content of EV released during different cell death modalities during necroptosis (Gupta et al., 2022; Shlomovitz et al., 2021), heat shock (Y. Li et al., 2020), apoptosis (Y. Li et al., 2020; Park et al., 2018; Tucher et al., 2018) and ferroptosis (Brown et al., 2019; Ito et al., 2021; Kajiwara et al., 2022). Nonetheless, it remained difficult to establish a real comparison between these studies because of distinct purification schemes and different cell lines used.

In the present study, we performed mass spectrometric-based proteomics on SEC- and UC-purified EVs from a single model cell line undergoing cell death according to different modalities: apoptosis, necroptosis, and ferroptosis. However, as revealed by WB in Figure S2c, TNF-stimulated cells were purely necroptotic (no activation of caspases), while anti-Fas-induced cells revealed apoptotic and necroptotic (MLKL phosphorylation) biochemical features. Indeed, conditions where caspase-8 remains inactive anti-Fas stimulation can engage necrotic cell death as we published previously (Vercammen, Beyaert, et al., 1998). ML162-induced cell death resulted in ferroptosis with underlying apoptotic signature. The latter is probably due to lipid peroxidation and consecutive oxidative stress at the organelle fraction (ER, mitochondria) (von Krusenstiern et al., 2023) resulting in the engagement of the apoptotic machinery, as has been reported before (Hoon Hong et al., 2017; P. Wu et al., 2023). Interestingly, also the necroptotic pathway seems to be (partially) engaged, as illustrated by MLKL S345 phosphorylation, but not the formation of higher molecular weight forms of MLKL as is the case during necroptosis. This illustrates how initiation of cell death pathways can crosstalk with each other. Despite these mixed cell death signatures (apoptosis with underlying necroptosis and ferroptosis with underlying apoptosis and necroptosis) the PCA analysis revealed distinct clustering of the different cell death modalities. Moreover, besides a large overlap in protein enrichment patterns in between cdEVs and ssEVs, at different stringencies ($> 1,5$-fold difference, > 4-fold difference) distinct patterns were observed between TNF-, anti-Fas- and ML162-induced RCD.

We found that the number of cdEVs released in each RCD modality was always increased albeit not significantly when compare to steady-state, as was previously reported for apoptosis (Distler et al., 2005). These cdEVs have a similar median size (100–110 nm), express identical EV markers (Alix, TSG101, CD81, Flottulin-1, Histone H3b, CD63, LAMP1), and contain a largely similar cargo composition. Surprisingly, the principal shared proteins in the cdEVs following low stringency analysis are an enrichment in proteins involved in ribosome biogenesis, RNA splicing, spliceosome, RNP complex formation and nuclear RNA transport. Besides a vast overlap, some exclusive enrichments were revealed in particular cdEVs by stringent analysis, suggesting that these processes may be preferentially targeted during apoptosis (ribosome biogenesis, rRNA processing and metabolism), necroptosis (ribosome biogenesis, (m)RNA catabolism), and ferroptosis (fatty acid β-oxidation, tRNA processing) (Figure S5d-f). In line with a prominence of GO terms associated with RNA-related processes, we documented an enrichment of rRNAs in EVs and revealed they are differentially 2′-O methylated compared to ssEVs. Such distinct rRNA modification profile may represent an adaptive response following cell death induction, with the potential to rewire translation. Importantly, parallel analysis of

rRNA methylation profiles in producing cells, indicated that the presence of differentially modified rRNA in vesicles was not a simple reflection of random sampling of cytoplasm of cells committed to programmed death but was due to a specific enrichment by a mechanism that remains to be established.

The International Society for Extracellular Vesicles states: "Especially important for EV studies is that the percent of dead cells at the time of EV harvest should be indicated since even a small percentage of cell death could release cell membranes that outnumber true released EVs. In addition, quantifying the percentage of apoptotic and necrotic cells may also be useful" (Théry et al., 2018). With regard to the cell death number, in all conditions analyzed in this work, the percentage of dead cells was comparable and of about 50% (Figure 1c). In practice, calnexin or calreticulin are evaluated as markers to exclude ongoing cell death and consecutive contamination by Golgi apparatus- and ER-associated proteins. Our cdEV analysis did not reveal any calreticulin or calnexin enrichment, in line with a recent report on EV content following necroptosis (Gupta et al., 2022). This shows that calnexin and calreticulin presence in EVs cannot be used as markers to assess cell death contamination. Furthermore, the absence of calnexin and calreticulin that the combination of SEC and UC indicates good quality EV preparation according to the MISEV guidelines (Théry et al., 2018). Larger EVs (often referred to as microvesicles and apoptotic bodies) were also reported during apoptosis (M. Li et al., 2020; Schiller et al., 2012; Wickman et al., 2013), necroptosis (Gong et al., 2017), or ferroptosis (Kajiwara et al., 2022), suggesting that exosome biogenesis is not the only pathway enhanced during RCD. Furthermore, following the current recommendation regarding EV characterization (Théry et al., 2018), the CD63 presence in necEVs and apoEVs indicates that necroptosis and apoptosis in L929 are mainly secreting exosomes. This observation corroborates recent reports in which similar EVs were reported to be released in necroptosis (Shlomovitz et al., 2021; Yoon et al., 2017; Zargarian et al., 2017), apoptosis (Park et al., 2018; Tucher et al., 2018), and ferroptosis (Brown et al., 2019; Ito et al., 2021; Kajiwara et al., 2022), altogether indicating that these RCD mainly enhances the release of exosome-like vesicles with a median size of 100 – 110 nm.

In the present work, cdEVs released following different RCD modalities exhibit strong similarities in biophysical properties and protein composition, suggesting the involvement of a common pathway in their biogenesis and cargo loading. Here, we reported the presence of tetraspanin (CD63, CD81), lipid raft-associated proteins flotillin-1 and -2, and ESCRT-III components (CHMP2-A and -B), in agreement with previous reports on apoptotic (Park et al., 2018; Tucher et al., 2018), necroptotic (Gupta et al., 2022; Shlomovitz et al., 2021; Yoon et al., 2017; Zargarian et al., 2017) and ferroptotic EVs (Brown et al., 2019; Ito et al., 2021; Kajiwara et al., 2022). However, the amount of these classically used exosomal markers (CD63, CD81, CHMP2A, CHMP2B, CHMP4B, CHMP4C, TSG101, FLOT1, FLOT2, Alix, nSMase) was quite similar between the different cdEVs, and they were relatively underrepresented in cdEVs compared to ssEVs, as revealed by proteomics. This was not the case for the presence of a cytosolic (GAPDH) or cytoskeleton (actin B) marker (Figure 2f). This would indicate that while the proteins involved in exosome formation remain rather constant, they are distributed over more vesicles in cdEVs compared to ssEVs. The sampling and cargo in the vesicles are increased, as reflected by the higher total protein content (Figure S1f).

The proteomic analysis revealed that most enriched proteins are related to RNA-binding and RNA-metabolism. EVs (microvesicles and exosomes) carry nucleic acids and various RNAs (Skog et al., 2008; Valadi et al., 2007) often referred to as extracellular RNA (exRNA), which is thought to be the most effective mechanism of cell-to-cell communication mediated by EVs (Das et al., 2019). The presence of RNA-binding proteins (RBP) facilitates RNA transport in exosomes (Statello et al., 2018; Wozniak et al., 2020). Its presence was already reported in apoEVs, in which components of the spliceosomes contribute to the intercellular transfer of splicing factors (Pavlyukov et al., 2018). The commonly shared enrichment between all three-cell death EVs according to the low stringent analysis (ribosome biogenesis, RNA splicing, RNP complexes, RNA transport and localization, and RNA export from the nucleus) (Figure S3d) could be a sign of rapid perturbation of spliceosome-related processes and nuclear RNA export during any RCD type. The concealing effect of EVs may prevent nucleic acid sensing responses and temper associated inflammatory signalling against spliceosomes and associated factors (Chang et al., 2021). In that respect the stringent analysis revealed a bias towards the exclusive enrichment of proteins involved in ribosome biogenesis, rRNA metabolic processing, and (m)RNA catabolic processes in the case of apoEVs and necEVs but not ferEVs. This indicates that these pathways may be preferentially regulated in apoptosis and necroptosis, but not in ferroptosis.

An important aspect of our study is that we reveal for the first time a distinctive rRNA methylation signature in cdEVs. This cell death fingerprint was in the form of nine hypomodified positions, two on the small ribosomal subunit (SSU-Um355, SSU-Cm1272) and seven on the large subunit (LSU-Am1137, LSU-Cm1154, LSU-Cm2120, LSU-Cm2177, LSU-Am3441, LSU-Am3523, and LSU-Cm3704) (Figure 4a-b). In particular, LSU-Am3441 is situated next to the peptidyl transferase centre (PTC), where amino acids are joined. Also interesting is the observation that the variable positions SSU-Cm1272 and LSU-Cm3704 are flanking the mRNA channel. Furthermore, we find it particularly striking that some of the 15 variable positions identified were also reported to vary during embryogenesis, where cell death is known to play a particularly critical role in tissue remodelling and morphogenesis. In particular, SSU-Um355 (equivalent to SSU-Um354 in humans) and SSU-Gm868 (SSU-Gm867) became more methylated in adult mice tissue when compared to E9.5 tissue (Hebras et al., 2020), and SSU-Um355 (SSU-Um354), SSU-Cm1272, LSU-Gm3600 (LSU-Gm3944) and LSU-Cm3704 (LSU-Cm4054) become more methylated as zebrafish embryonic development advances (Ramachandran et al., 2020). At this stage, we have shown that differentially modified rRNAs are detected in all three cell death EVs. Therefore, it is tempting to speculate that these differentially methylated rRNAs are involved in regulating cell death and in the cell-to-cell transmission of information. Such a model is particularly appealing when considering that parallel

RiboMethSeq analysis conducted in matched cell bodies from rRNA-producing cells revealed the enrichment in vesicles is highly specific. It is important to note that the changes in rRNA methylation reported could not simply be explained by lower rRNA input in the analysis of EV samples because the affected positions lie in rRNA segments that contain multiple other 2′-O methylations that remain unchanged.

In conclusion, we pioneered a systematic analysis of protein and ribomethylated rRNA composition of EVs produced during apoptosis, necroptosis, and ferroptosis in a single model cell line. We showed that cell death leads to increased protein content of EVs mainly enriched in proteins involved in ribosome biogenesis and rRNA processing in apoEVs and necEVs, while protein enrichment involved in RNA splicing, RNP complexes, RNA transport, and localization, RNA nuclear export as well as differentially methylated rRNA, define a common EV fingerprint between all three RCD modalities. Our report points toward the importance of sorting RNA-related processes into EVs during cell death, a topic of considerable interest as its functional consequences remain largely unknown (Fabbiano et al., 2020; O'Brien et al., 2020).

AUTHOR CONTRIBUTIONS

Benjamin Cappe: Conceptualization; data curation; formal analysis; investigation; methodology; writing—original draft. **Mike Vadi**: Investigation; resources; validation; writing—review and editing. **Eliza Sack**: Investigation; methodology; visualization. **Ludivine Wacheul**: Investigation; methodology; visualization. **Bruno Verstraeten**: Data curation; formal analysis; visualization; writing—review and editing. **Sara Dufour**: Formal analysis; investigation; methodology. **Wei Xie**: Conceptualization; supervision; writing—review and editing. **Julien Franck**: Data curation; formal analysis. **Francis Impens**: Investigation; methodology; supervision; writing—review and editing. **An Hendrix**: Conceptualization; supervision; data interpretation. **Denis L.J. Lafontaine**: Data curation; investigation; methodology; writing—review and editing. **Peter Vandenabeele**: Conceptualization; funding acquisition; project administration; resources; supervision; writing—original draft; writing—review and editing. **Franck Riquet**: Conceptualization; supervision; writing—original draft; writing-review and editing.

ACKNOWLEDGEMENTS

CONFLICT OF INTEREST STATEMENT

The authors declare no conflicts of interest.

ORCID

Benjamin Cappe https://orcid.org/0000-0002-8162-9788
Denis L. J. Lafontaine https://orcid.org/0000-0001-7295-6288
Peter Vandenabeele https://orcid.org/0000-0002-6669-8822
Franck B. Riquet https://orcid.org/0000-0001-8417-4283

REFERENCES

Battistelli, M., & Falcieri, E. (2020). Apoptotic bodies: Particular extracellular vesicles involved in intercellular communication. *Biology*, *9*(1), 21. https://doi.org/10.3390/biology9010021

Bedoui, S., Herold, M. J., & Strasser, A. (2020). Emerging connectivity of programmed cell death pathways and its physiological implications. *In Nature Reviews Molecular Cell Biology*, *21*(11), 678–695. Nature Research. https://doi.org/10.1038/s41580-020-0270-8

Brock, C. K., Wallin, S. T., Ruiz, O. E., Samms, K. M., Mandal, A., Sumner, E. A., & Eisenhoffer, G. T. (2019). Stem cell proliferation is induced by apoptotic bodies from dying cells during epithelial tissue maintenance. *Nature Communications*, *10*(1), 1044. https://doi.org/10.1038/s41467-019-09010-6

Brown, C. W., Amante, J. J., Chhoy, P., Elaimy, A. L., Liu, H., Zhu, L. J., Baer, C. E., Dixon, S. J., & Mercurio, A. M. (2019). Prominin2 drives ferroptosis resistance by stimulating iron export. *Developmental Cell*, *51*(5), 575–586.e4. https://doi.org/10.1016/J.DEVCEL.2019.10.007

Buzas, E. I. (2022). The roles of extracellular vesicles in the immune system. *Nature Reviews. Immunology*, 1–15. https://doi.org/10.1038/s41577-022-00763-8

Chang, A. Y., Zhou, Y. J., Iyengar, S., Pobiarzyn, P. W., Tishchenko, P., Shah, K. M., Wheeler, H., Wang, Y.-M., Loria, P. M., Loganzo, F., & Woo, S.-R. (2021). Modulation of SF3B1 in the pre-mRNA spliceosome induces a RIG-I-dependent type I IFN response. *Journal of Biological Chemistry*, *297*(5), 101277. https://doi.org/10.1016/j.jbc.2021.101277

Das, S., Abdel-Mageed, A. B., Adamidi, C., Adelson, P. D., Akat, K. M., Alsop, E., Ansel, K. M., Arango, J., Aronin, N., Avsaroglu, S. K., Azizian, A., Balaj, L., Ben-Dov, I. Z., Bertram, K., Bitzer, M., Blelloch, R., Bogardus, K. A., Breakefield, X. O., Calin, G. A., … Saugstad, J. A. (2019). The extracellular RNA communication consortium: establishing foundational knowledge and technologies for extracellular RNA research. *Cell*, *177*(2), 231. https://doi.org/10.1016/J.CELL.2019.03.023

Delhermite, J., Tafforeau, L., Sharma, S., Marchand, V., Wacheul, L., Lattuca, R., Desiderio, S., Motorin, Y., Bellefroid, E., & Lafontaine, D. L. J. (2022). Systematic mapping of rRNA 2'-O methylation during frog development and involvement of the methyltransferase Fibrillarin in eye and craniofacial development in Xenopus laevis. *PLOS Genetics*, *18*(1), e1010012. https://doi.org/10.1371/journal.pgen.1010012

Distler, J. H. W., Huber, L. C., Hueber, A. J., Reich, C. F., Gay, S., Distler, O., & Pisetsky, D. S. (2005). The release of microparticles by apoptotic cells and their effects on macrophages. *Apoptosis*, *10*(4), 731–741. https://doi.org/10.1007/s10495-005-2941-5

Duprez, L., Takahashi, N., Van Hauwermeiren, F., Vandendriessche, B., Goossens, V., Vanden Berghe, T., Declercq, W., Libert, C., Cauwels, A., & Vandenabeele, P. (2011). RIP kinase-dependent necrosis drives lethal systemic inflammatory response syndrome. *Immunity*, *35*(6), 908–918. https://doi.org/10.1016/j.immuni.2011.09.020

Fabbiano, F., Corsi, J., Gurrieri, E., Trevisan, C., Notarangelo, M., & D'Agostino, V. G. (2020). RNA packaging into extracellular vesicles: An orchestra of RNA-binding proteins? *Journal of Extracellular Vesicles*, *10*(2), e12043. https://doi.org/10.1002/JEV2.12043

Gay, D. M., Lund, A. H., & Jansson, M. D. (2022). Translational control through ribosome heterogeneity and functional specialization. *Trends in Biochemical Sciences*, *47*(1), 66–81. https://doi.org/10.1016/j.tibs.2021.07.001

Genuth, N. R., & Barna, M. (2018a). Heterogeneity and specialized functions of translation machinery: From genes to organisms. *Nature Reviews Genetics*, *19*(7), 431–452. https://doi.org/10.1038/s41576-018-0008-z

Genuth, N. R., & Barna, M. (2018b). The discovery of ribosome heterogeneity and its implications for gene regulation and organismal life. *Molecular Cell*, *71*(3), 364–374. https://doi.org/10.1016/j.molcel.2018.07.018

Gong, Y., Guy, C., Olauson, H., Becker, J. U., Yang, M., Fitzgerald, P., Linkermann, A., & Green, D. R. (2017). ESCRT-III acts downstream of MLKL to regulate necroptotic cell death and its consequences. *Cell*, *169*(2), 286–300.e16. https://doi.org/10.1016/j.cell.2017.03.020

Gupta, K., Brown, K. A., Hsieh, M. L., Hoover, B. M., Wang, J., Khoury, M. K., Pilli, V. S. S., Beyer, R. S. H., Voruganti, N. R., Chaudhary, S., Roberts, D. S., Murphy, R. M., Hong, S., Ge, Y., & Liu, B. (2022). Necroptosis is associated with Rab27-independent expulsion of extracellular vesicles containing RIPK3 and MLKL. *Journal of Extracellular Vesicles*, *11*(9), e12261. https://doi.org/10.1002/JEV2.12261

Hebras, J., Krogh, N., Marty, V., Nielsen, H., & Cavaillé, J. (2020). Developmental changes of rRNA ribose methylations in the mouse. *RNA Biology*, *17*(1), 150–164. https://doi.org/10.1080/15476286.2019.1670598

Hoon Hong, S., Lee, D.-H., Lee, Y.-S., Jee Jo, M., Jeong, Y. A., Kwon, W. T., Choudry, H. A., Bartlett, D. L., & Lee, Y. J. (2017). Molecular crosstalk between ferroptosis and apoptosis: emerging role of ER stress-induced p53-independent PUMA expression. www.impactjournals.com/oncotarget

Hu, Z.-L., Bao, J., & Reecy, J. (2008). CateGOrizer: A web-based program to batch analyze gene ontology classification categories. *Online Journal of Bioinformatics*, *9*(2), 108–112. http://users.comcen.com.au/~journals/geneontologyabs2008.htm

Huang, D. W., Sherman, B. T., & Lempicki, R. A. (2009a). Bioinformatics enrichment tools: Paths toward the comprehensive functional analysis of large gene lists. *Nucleic Acids Research*, *37*(1), 1–13. https://doi.org/10.1093/nar/gkn923

Huang, D. W., Sherman, B. T., & Lempicki, R. A. (2009b). Systematic and integrative analysis of large gene lists using DAVID bioinformatics resources. *Nature Protocols*, *4*(1), 44–57. https://doi.org/10.1038/nprot.2008.211

Ito, F., Kato, K., Yanatori, I., Murohara, T., & Toyokuni, S. (2021). Ferroptosis-dependent extracellular vesicles from macrophage contribute to asbestos-induced mesothelial carcinogenesis through loading ferritin. *Redox Biology*, *47*, 102174. https://doi.org/10.1016/J.REDOX.2021.102174

Kajiwara, K., Beharier, O., Chng, C.-P., Goff, J. P., Ouyang, Y., St Croix, C. M., Huang, C., Kagan, V. E., Hsia, K. J., & Sadovsky, Y. (2022). Ferroptosis induces membrane blebbing in placental trophoblasts. *Journal of Cell Science*, *135*(5), jcs255737. https://doi.org/10.1242/jcs.255737

Kakarla, R., Hur, J., Kim, Y. J., Kim, J., & Chwae, Y. J. (2020). Apoptotic cell-derived exosomes: messages from dying cells. *In Experimental and Molecular Medicine*, *52*, 1–6. Springer Nature. https://doi.org/10.1038/s12276-019-0362-8

Kalra, H., Simpson, R. J., Ji, H., Aikawa, E., Altevogt, P., Askenase, P., Bond, V. C., Borràs, F. E., Breakefield, X., Budnik, V., Buzas, E., Camussi, G., Clayton, A., Cocucci, E., Falcon-Perez, J. M., Gabrielsson, S., Gho, Y. S., Gupta, D., Harsha, H. C., … Mathivanan, S. (2012). Vesiclepedia: A compendium for extracellular vesicles with continuous community annotation. *PLOS Biology*, *10*(12), e1001450. https://doi.org/10.1371/JOURNAL.PBIO.1001450

Keerthikumar, S., Chisanga, D., Ariyaratne, D., al Saffar, H., Anand, S., Zhao, K., Samuel, M., Pathan, M., Jois, M., Chilamkurti, N., Gangoda, L., & Mathivanan, S. (2016). ExoCarta: A web-based compendium of exosomal cargo. *Journal of Molecular Biology*, *428*(4), 688–692. https://doi.org/10.1016/j.jmb.2015.09.019

Kim, R., Hashimoto, A., Markosyan, N., Tyurin, V. A., Tyurina, Y. Y., Kar, G., Fu, S., Sehgal, M., Garcia-Gerique, L., Kossenkov, A., Gebregziabher, B. A., Tobias, J. W., Hicks, K., Halpin, R. A., Cvetesic, N., Deng, H., Donthireddy, L., Greenberg, A., Nam, B., … Gabrilovich, D. I. (2022). Ferroptosis of tumour neutrophils causes immune suppression in cancer. *Nature*, *612*(7939), 338–346. https://doi.org/10.1038/s41586-022-05443-0

Lamparski, H. G., Metha-Damani, A., Yao, J. Y., Patel, S., Hsu, D. H., Ruegg, C., & le Pecq, J. B. (2002). Production and characterization of clinical grade exosomes derived from dendritic cells. *Journal of Immunological Methods*, *270*(2). https://doi.org/10.1016/S0022-1759(02)00330-7

Larios, J., Mercier, V., Roux, A., & Gruenberg, J. (2020). ALIX- And ESCRT-III-dependent sorting of tetraspanins to exosomes. *Journal of Cell Biology*, *219*(3), e201904113. https://doi.org/10.1083/jcb.201904113

Li, J., van Vranken, J. G., Vaites, L. P., Schweppe, D. K., Huttlin, E. L., Etienne, C., Nandhikonda, P., Viner, R., Robitaille, A. M., Thompson, A. H., Kuhn, K., Pike, I., Bomgarden, R. D., Rogers, J. C., Gygi, S. P., & Paulo, J. A. (2020). TMTpro reagents: a set of isobaric labeling mass tags enables simultaneous proteome-wide measurements across 16 samples. *Nature Methods*, *17*(4), 399–404. https://doi.org/10.1038/s41592-020-0781-4

Li, M., Liao, L., & Tian, W. (2020). Extracellular vesicles derived from apoptotic cells: An essential link between death and regeneration. *Frontiers in Cell and Developmental Biology*, *8*, 1063. https://doi.org/10.3389/FCELL.2020.573511/BIBTEX

Li, Y., Zhu, X., Wang, G., Tong, H., Su, L., & Li, X. (2020). Proteomic analysis of extracellular vesicles released from heat-stroked hepatocytes reveals promotion of programmed cell death pathway. *Biomedicine & Pharmacotherapy*, *129*, 110489. https://doi.org/10.1016/J.BIOPHA.2020.110489

Marcel, V., Ghayad, S. E., Belin, S., Therizols, G., Morel, A.-P., Solano-Gonzàlez, E., Vendrell, J. A., Hacot, S., Mertani, H. C., Albaret, M. A., Bourdon, J.-C., Jordan, L., Thompson, A., Tafer, Y., Cong, R., Bouvet, P., Saurin, J.-C., Catez, F., Prats, A.-C., … Diaz, J.-J. (2013). p53 acts as a safeguard of translational control by regulating fibrillarin and rRNA methylation in cancer. *Cancer Cell*, *24*(3), 318–330. https://doi.org/10.1016/j.ccr.2013.08.013

Marchand, V., Ayadi, L., el Hajj, A., Blanloeil-Oillo, F., Helm, M., & Motorin, Y. (2017). High-Throughput Mapping of 2′-O-Me Residues in RNA Using Next-Generation Sequencing (Illumina RiboMethSeq Protocol, 171–187. https://doi.org/10.1007/978-1-4939-6807-7_12

Marchand, V., Blanloeil-Oillo, F., Helm, M., & Motorin, Y. (2016). Illumina-based RiboMethSeq approach for mapping of 2′-O-Me residues in RNA. *Nucleic Acids Research*, 44(16), e135–e135. https://doi.org/10.1093/nar/gkw547

Mathieu, M., Névo, N., Jouve, M., Valenzuela, J. I., Maurin, M., Verweij, F. J., Palmulli, R., Lankar, D., Dingli, F., Loew, D., Rubinstein, E., Boncompain, G., Perez, F., & Théry, C. (2021). Specificities of exosome versus small ectosome secretion revealed by live intracellular tracking of CD63 and CD9. *Nature Communications*, 12, 4389. https://doi.org/10.1038/s41467-021-24384-2

Mathivanan, S., Fahner, C. J., Reid, G. E., & Simpson, R. J. (2012). ExoCarta 2012: Database of exosomal proteins, RNA and lipids. *Nucleic Acids Research*, 40(D1), D1241–D1244. https://doi.org/10.1093/nar/gkr828

McAndrews, K. M., & Kalluri, R. (2019). Mechanisms associated with biogenesis of exosomes in cancer. In *Molecular Cancer*, 18, 52. BioMed Central Ltd. https://doi.org/10.1186/s12943-019-0963-9

McQuin, C., Goodman, A., Chernyshev, V., Kamentsky, L., Cimini, B. A., Karhohs, K. W., Doan, M., Ding, L., Rafelski, S. M., Thirstrup, D., Wiegraebe, W., Singh, S., Becker, T., Caicedo, J. C., & Carpenter, A. E. (2018). CellProfiler 3.0: Next-generation image processing for biology. *PLOS Biology*, 16(7), e2005970. https://doi.org/10.1371/JOURNAL.PBIO.2005970

Meckes, D. G., & Raab-Traub, N. (2011). Microvesicles and viral infection. *Journal of Virology*, 85(24), 12844–12854. https://doi.org/10.1128/jvi.05853-11

Metzner, C., & Zaruba, M. (2021). On the relationship of viral particles and extracellular vesicles: Implications for viral vector technology. *Viruses*, 13(7), 1238. https://doi.org/10.3390/v13071238

Mir, B., & Goettsch, C. (2020). Extracellular vesicles as delivery vehicles of specific cellular cargo. *In Cells*, 9(7), 1601. https://doi.org/10.3390/cells9071601

O'Brien, K., Breyne, K., Ughetto, S., Laurent, L. C., & Breakefield, X. O. (2020). RNA delivery by extracellular vesicles in mammalian cells and its applications. *Nature Reviews Molecular Cell Biology*, 21(10), 585–606. https://doi.org/10.1038/s41580-020-0251-y

Panzilius, E., Holstein, F., Dehairs, J., Planque, M., Toerne, C. V., Koenig, A.-C., Doll, S., Bannier-Hélaouët, M., Ganz, H. M., Hauck, S. M., Talebi, A., Swinnen, J. v., Fendt, S.-M., Angeli, J. P. F., Conrad, M., & Scheel, C. H. (2019). Cell density-dependent ferroptosis in breast cancer is induced by accumulation of polyunsaturated fatty acid-enriched triacylglycerides. *BioRxiv*, 417949. https://doi.org/10.1101/417949

Park, S. J., Kim, J. M., Kim, J., Hur, J., Park, S., Kim, K., Shin, H. J., & Chwae, Y. J. (2018). Molecular mechanisms of biogenesis of apoptotic exosome-like vesicles and their roles as damage-associated molecular patterns. *Proceedings of the National Academy of Sciences of the United States of America*, 115(50), E11721–E11730. https://doi.org/10.1073/pnas.1811432115

Pathan, M., Fonseka, P., Chitti, S. v., Kang, T., Sanwlani, R., van Deun, J., Hendrix, A., & Mathivanan, S. (2019). Vesiclepedia 2019: A compendium of RNA, proteins, lipids and metabolites in extracellular vesicles. *Nucleic Acids Research*, 47(D1), D516–D519. https://doi.org/10.1093/nar/gky1029

Pavlyukov, M. S., Yu, H., Bastola, S., Minata, M., Shender, V. O., Lee, Y., Zhang, S., Wang, J., Komarova, S., Wang, J., Yamaguchi, S., Alsheikh, H. A., Shi, J., Chen, D., Mohyeldin, A., Kim, S. H., Shin, Y. J., Anufrieva, K., Evtushenko, E. G., … Nakano, I. (2018). Apoptotic cell-derived extracellular vesicles promote malignancy of glioblastoma via intercellular transfer of splicing factors. *Cancer Cell*, 34(1), 119–135.e10. https://doi.org/10.1016/j.ccell.2018.05.012

Ramachandran, S., Krogh, N., Jørgensen, T. E., Johansen, S. D., Nielsen, H., & Babiak, I. (2020). The shift from early to late types of ribosomes in zebrafish development involves changes at a subset of rRNA 2′-O-Me sites. *RNA*, 26(12), 1919–1934. https://doi.org/10.1261/rna.076760.120

Ritchie, M. E., Phipson, B., Wu, D., Hu, Y., Law, C. W., Shi, W., & Smyth, G. K. (2015). Limma powers differential expression analyses for RNA-sequencing and microarray studies. *Nucleic Acids Research*, 43(7), e47. https://doi.org/10.1093/nar/gkv007

Schiller, M., Parcina, M., Heyder, P., Foermer, S., Ostrop, J., Leo, A., Heeg, K., Herrmann, M., Lorenz, H.-M., & Bekeredjian-Ding, I. (2012). Induction of type I IFN is a physiological immune reaction to apoptotic cell-derived membrane microparticles. *The Journal of Immunology*, 189(4), 1747–1756. https://doi.org/10.4049/jimmunol.1100631

Sharma, S., & Lafontaine, D. L. J. (2015). 'View From A Bridge': A new perspective on eukaryotic rRNA base modification. *Trends in Biochemical Sciences*, 40(10), 560–575. https://doi.org/10.1016/j.tibs.2015.07.008

Sharma, S., Marchand, V., Motorin, Y., & Lafontaine, D. L. J. (2017). Identification of sites of 2′-O-methylation vulnerability in human ribosomal RNAs by systematic mapping. *Scientific Reports*, 7(1), 11490. https://doi.org/10.1038/s41598-017-09734-9

Shlomovitz, I., Erlich, Z., Arad, G., Edry-Botzer, L., Zargarian, S., Cohen, H., Manko, T., Ofir-Birin, Y., Cooks, T., Regev-Rudzki, N., & Gerlic, M. (2021). Proteomic analysis of necroptotic extracellular vesicles. *Cell Death & Disease*, 12(11), 1059. https://doi.org/10.1038/s41419-021-04317-z

Skog, J., Würdinger, T., van Rijn, S., Meijer, D. H., Gainche, L., Curry, W. T., Carter, B. S., Krichevsky, A. M., & Breakefield, X. O. (2008). Glioblastoma microvesicles transport RNA and proteins that promote tumour growth and provide diagnostic biomarkers. *Nature Cell Biology*, 10(12), 1470–1476. https://doi.org/10.1038/NCB1800

Statello, L., Maugeri, M., Garre, E., Nawaz, M., Wahlgren, J., Papadimitriou, A., Lundqvist, C., Lindfors, L., Collén, A., Sunnerhagen, P., Ragusa, M., Purrello, M., Pietro, C. di, Tigue, N., & Valadi, H. (2018). Identification of RNA-binding proteins in exosomes capable of interacting with different types of RNA: RBP-facilitated transport of RNAs into exosomes. *PLoS ONE*, 13(4), 1–30. https://doi.org/10.1371/journal.pone.0195969

Sun, L., Wang, H., Wang, Z., He, S., Chen, S., Liao, D., Wang, L., Yan, J., Liu, W., Lei, X., & Wang, X. (2012). Mixed lineage kinase domain-like protein mediates necrosis signaling downstream of RIP3 kinase. *Cell*, 148(1–2), 213–227. https://doi.org/10.1016/j.cell.2011.11.031

Théry, C., Witwer, K. W., Aikawa, E., Alcaraz, M. J., Anderson, J. D., Andriantsitohaina, R., Antoniou, A., Arab, T., Archer, F., Atkin-Smith, G. K., Ayre, D. C., Bach, J. M., Bachurski, D., Baharvand, H., Balaj, L., Baldacchino, S., Bauer, N. N., Baxter, A. A., Bebawy, M., … Zuba-Surma, E. K. (2018). Minimal information for studies of extracellular vesicles 2018 (MISEV2018): A position statement of the International Society for Extracellular Vesicles and update of the MISEV2014 guidelines. *Journal of Extracellular Vesicles*, 7(1), 1535750. https://doi.org/10.1080/20013078.2018.1535750

Tucher, C., Bode, K., Schiller, P., Claßen, L., Birr, C., Souto-Carneiro, M. M., Blank, N., Lorenz, H. M., & Schiller, M. (2018). Extracellular vesicle subtypes released from activated or apoptotic T-lymphocytes carry a specific and stimulus-dependent protein cargo. *Frontiers in Immunology*, 9(MAR), 534. https://doi.org/10.3389/fimmu.2018.00534

Valadi, H., Ekström, K., Bossios, A., Sjöstrand, M., Lee, J. J., & Lötvall, J. O. (2007). Exosome-mediated transfer of mRNAs and microRNAs is a novel mechanism of genetic exchange between cells. *Nature Cell Biology*, 9(6), 654–659. https://doi.org/10.1038/ncb1596

van den Akker, G. G. H., Caron, M. M. J., Peffers, M. J., & Welting, T. J. M. (2022). Ribosome dysfunction in osteoarthritis. *Current Opinion in Rheumatology*, 34(1), 61–67. https://doi.org/10.1097/BOR.0000000000000858

Van Deun, J., Mestdagh, P., de Wever, O., Vergauwen, G., Vandesompele, J., & Hendrix, A. (2017). EV-TRACK: Transparent reporting and centralizing knowledge in EV research. *Nat Methods*, 14(3), 228–232. www.evtrack.org

van Niel, G., Carter, D. R. F., Clayton, A., Lambert, D. W., Raposo, G., & Vader, P. (2022). Challenges and directions in studying cell–cell communication by extracellular vesicles. *Nature Reviews Molecular Cell Biology*, 23, 369–382. https://doi.org/10.1038/s41580-022-00460-3

van Niel, G., D'Angelo, G., & Raposo, G. (2018). Shedding light on the cell biology of extracellular vesicles. In *Nature Reviews Molecular Cell Biology*, 19(4), 213–228. Nature Publishing Group. https://doi.org/10.1038/nrm.2017.125

Vercammen, D., Beyaert, R., Denecker, G., Goossens, V., Van Loo, G., Declercq, W., Grooten, J., Fiers, W., & Vandenabeele, P. (1998). Inhibition of caspases increases the sensitivity of L929 cells to necrosis mediated by tumor necrosis factor. *The Journal of Experimental Medicine*, *187*(9), 1477–1485. https://doi.org/10.1084/jem.187.9.1477

Vercammen, D., Brouckaert, G., Denecker, G., Van de Craen, M., Declercq, W., Fiers, W., & Vandenabeele, P. (1998). Dual signaling of the Fas receptor: Initiation of both apoptotic and necrotic cell death pathways. *The Journal of Experimental Medicine*, *188*(5), 919–930. https://doi.org/10.1084/jem.188.5.919

von Krusenstiern, A. N., Robson, R. N., Qian, N., Qiu, B., Hu, F., Reznik, E., Smith, N., Zandkarimi, F., Estes, V. M., Dupont, M., Hirschhorn, T., Shchepinov, M. S., Min, W., Woerpel, K. A., & Stockwell, B. R. (2023). Identification of essential sites of lipid peroxidation in ferroptosis. *Nature Chemical Biology*, *19*(6), 719–730. https://doi.org/10.1038/s41589-022-01249-3

Wallach, D., Kang, T.-B., Dillon, C. P., & Green, D. R. (2016). Programmed necrosis in inflammation: Toward identification of the effector molecules. *Science*, *352*(6281), aaf2154–aaf2154. https://doi.org/10.1126/science.aaf2154

Wickman, G. R., Julian, L., Mardilovich, K., Schumacher, S., Munro, J., Rath, N., Zander, S. A., Mleczak, A., Sumpton, D., Morrice, N., Bienvenut, W. v., & Olson, M. F. (2013). Blebs produced by actin-myosin contraction during apoptosis release damage-associated molecular pattern proteins before secondary necrosis occurs. *Cell Death and Differentiation*, *20*(10), 1293–1305. https://doi.org/10.1038/cdd.2013.69

Wiernicki, B., Maschalidi, S., Pinney, J., Adjemian, S., vanden Berghe, T., Ravichandran, K. S., & Vandenabeele, P. (2022). Cancer cells dying from ferroptosis impede dendritic cell-mediated anti-tumor immunity. *Nature Communications*, *13*(1), 3676. https://doi.org/10.1038/s41467-022-31218-2

Wozniak, A. L., Adams, A., King, K. E., Dunn, W., Christenson, L. K., Hung, W. T., & Weinman, S. A. (2020). The RNA binding protein FMR1 controls selective exosomal miRNA cargo loading during inflammation. *Journal of Cell Biology*, 219(10). https://doi.org/10.1083/JCB.201912074/152116

Wu, P., Zhang, X., Duan, D., & Zhao, L. (2023). Organelle-specific mechanisms in crosstalk between apoptosis and ferroptosis. In *Oxidative Medicine and Cellular Longevity*, 2023. Hindawi Limited. https://doi.org/10.1155/2023/3400147

Wu, T., Hu, E., Xu, S., Chen, M., Guo, P., Dai, Z., Feng, T., Zhou, L., Tang, W., Zhan, L., Fu, X., Liu, S., Bo, X., & Yu, G. (2021). clusterProfiler 4.0: A universal enrichment tool for interpreting omics data. *The Innovation*, *2*(3), 100141. https://doi.org/10.1016/j.xinn.2021.100141

Yoon, S., Kovalenko, A., Bogdanov, K., & Wallach, D. (2017). MLKL, the protein that mediates necroptosis, also regulates endosomal trafficking and extracellular vesicle generation. *Immunity*, *47*(1), 51–65.e7. https://doi.org/10.1016/j.immuni.2017.06.001

Zargarian, S., Shlomovitz, I., Erlich, Z., Hourizadeh, A., Ofir-Birin, Y., Croker, B. A., Regev-Rudzki, N., Edry-Botzer, L., & Gerlic, M. (2017). Phosphatidylserine externalization, "necroptotic bodies" release, and phagocytosis during necroptosis. *PLoS Biology*, *15*(6), 1–23. https://doi.org/10.1371/journal.pbio.2002711

Zhang, X., Smits, A. H., van Tilburg, G. B. A., Ovaa, H., Huber, W., & Vermeulen, M. (2018). Proteome-wide identification of ubiquitin interactions using UbIA-MS. *Nature Protocols*, *13*(3), 530–550. https://doi.org/10.1038/nprot.2017.147

SUPPORTING INFORMATION

Additional supporting information can be found online in the Supporting Information section at the end of this article.